Spatial Compounding and Segmentation of Volumetric Ultrasound Data Sets for Generating Interactive Anatomic Models

by

Jeremy Wynne Cannon

B.S., Biochemistry (1994)
United States Air Force Academy

M.D. (1998)
Harvard University

Submitted to the Department of Mechanical Engineering
in Partial Fulfillment of the Requirements for the Degree of

Master of Science in Mechanical Engineering

at the

MASSACHUSETTS INSTITUTE OF TECHNOLOGY

June 2003

Signature of Author .....
Department of Mechanical Engineering
May 9, 2003

Certified by .....
Derek Rowell
Professor of Mechanical Engineering
Thesis Supervisor

Certified by .....
Robert D. Howe
Gordon McKay Professor of Engineering
Division of Engineering and Applied Sciences, Harvard University
Thesis Supervisor

Accepted by .....
Ain A. Sonin
Chairman, Department Committee on Graduate Students

Spatial Compounding and Segmentation of Volumetric Ultrasound Data Sets for Generating Interactive Anatomic Models

by

Jeremy Wynne Cannon

Submitted to the Department of Mechanical Engineering on May 9, 2003
in Partial Fulfillment of the Requirements for the Degree of
Master of Science in Mechanical Engineering

Abstract

Surgical procedures guided by non-optical imaging represent a growing proportion of medical interventions. The goal of this type of approach is to reduce the invasiveness of current procedures or to treat disease using new procedures which would not possible without the assistance of medical imaging. The field of cardiac surgery represents a medical subspecialty where image-guided interventions could markedly improve current treatment methods. In particular, all surgical procedures performed inside the heart require the use of cardiopulmonary bypass and cardiac arrest even when performing these procedures using "minimally invasive" techniques. Side effects of this bypass process range from a mild inflammatory response to multi-organ dysfunction.

This thesis investigates the use of *real time* 3-D ultrasound (US) for possibly guiding surgical procedures inside the heart without using cardiopulmonary bypass. In a series of *in vivo* studies in an animal model and an *in vitro* tank study, the limitations of both 2-D US and 3-D US for guiding surgical tasks were systematically identified. These initial studies confirmed the inadequacy of 2-D US for guiding complicated surgical maneuvers and verified the utility of real time 3-D US for efficiently guiding both basic and more complex surgical tasks. However, several important problems with using US for guiding surgical procedures were identified.

First, because the surgeon is entirely dependent upon the US image for instrument positioning, additional safety measures are required to prevent inadvertent injuries. In addressing this problem, a computationally efficient active contour segmentation model was applied to the volumetric US images. This algorithm (developed recently by Perrin at the University of Minnesota) proved sufficiently fast to keep pace with the volumetric US data stream with good accuracy. Thus, this approach can be applied to establish a "virtual fixture" inside the heart wall during these surgical procedures to prevent injuries.

Another significant problem present during US guided procedures (2-D and 3-D) involves maintaining spatial orientation. With 3-D US-guided procedures, the image affords sufficient spatial cues to guide the procedure once the tools are within the imaging field of view. However, guiding the tools into view and keeping them there proves quite challenging. In addition, maintaining orientation relative to known anatomic landmarks during the procedure also proves challenging. To address these problems, a spatially compounded US image of the heart was produced and a graphical model was registered to this data set. Such a registered graphical model could be used as a navigational aid for the surgeon during image-guided procedures inside the beating heart.

Thesis Supervisor: Derek Rowell
Title: Professor of Mechanical Engineering

Biographical Note

Education

Massachusetts Institute of Technology Present
Candidate for S.M. in Mechanical Engineering
NIH Postdoctoral Research Fellow in Cardiovascular Surgery

Beth Israel Deaconess Medical Center 1998-2001
Resident in General Surgery

Harvard Medical School 1998
Doctor of Medicine

United States Air Force Academy 1994
Bachelor of Science in Biochemistry

Honors and Awards

Isaac O. Mehrez Award for Surgical Excellence 2001
Beth Israel Deaconess Medical Center Department of Surgery

Distinguished Graduate with Academic Honors 1994
Ranked 3/1026 in Academic Order of Merit, USAF Academy

National Society Daughters of the American Colonists Award 1994
Outstanding Student Achievement Award, Dept. of Chemistry, USAF Academy

Authorship

Cannon, J.W., Stoll J.A., Howe R.D., Salgo I.S., Knowles H.B., Dupont P.E., Marx G.R., del Nido P.J. Real time three-dimensional ultrasound for guiding surgical tasks. *Comput Aided Surg*. Accepted for Publication.

Cannon J.W., Howe R.D., Dupont P.E., Triedman J.K., Marx G.R., del Nido P.J. Application of robotics in congenital cardiac surgery. *Semin Thorac Cardiovasc Surg: Pediatric Cardiac Surgery Annual*. In Press.

Mihaljevic T, **Cannon J.W.**, del Nido P.J. Robotically-assisted division of a vascular ring in children. *J Thorac Cardiovasc Surg*. In press.

Cannon J.W., Stoll J.A., Selha S.D., Dupont P.E., Howe R.D., Torchiana D.F. Port placement planning in robot-assisted coronary artery bypass. *IEEE Tra Robot Automat*. In press.

Cannon J.W. A mathematical model of hemorrhagic shock: the future of trauma triage. *Mil Med*. 2002 Apr; 167(4):312-6.

Activities

Husband of 5 years to Jane and father to my new son Caleb Present

Endurance Sports
Wheelworks Multisport Triathlon Team, Belmont, MA Present
107th Boston Marathon 2003

Acknowledgments

From the first time I stepped foot in an operating room as a newly declared pre-med from a military academy, the high stakes drama of cardiac surgery has fascinated me. This profession represents an opportunity to experience the excitement of tremendous privilege that I never could have enjoyed as a fighter pilot. Ten years later, I am now well on my way to living this dream that has been so long in the making. This thesis and the accompanying degree will give me a special niche as I seek to uphold the cardiac surgeon's tradition of embracing technology for the good of their patients.

Along this difficult career path, many people have believed in me, encouraged me, and supported me with praise, prayer, and lots of good home-cooked meals. My wife Jane has been a model of dedication and deference. Thank you for everything: for noticing, for cheering, and for running with me. To Caleb, my new son, I want to be a good role model in contrast to the many sub-standard role models around in the world today. To my father and mother, thank you for your commitment to your family which led you to sacrifice so much. I only hope I can be as strong in tough times. To my new dad and mom Hal and Ann, thank you for the great vacations, for watching Caleb, and for all the thoughtful things you have done.

My cardiac surgery mentors Drs. Pedro del Nido, Frank Sellke, and Sid Levitsky are all in some way responsible for facilitating this project which has proven amazingly fun and very productive. You have all done so much for me that the only way I can repay you is to take good care of your patients in the ICUs and on the floor for the next *n* number of years! Dr. del Nido, I especially want to thank you for mentoring me as your research resident and for your amazing vision and motivation which laid the foundation for this research program. Dr. Marx, how can I ever thank you enough for all the time you spent imaging everything from my heart to all of our animal subjects. Drs. Fritz Johnson and J.D. Rogers from Springfield, MO, you all started this mess in the first place, and for that I am extremely grateful.

I now want to express my deep gratitude to the engineering faculty who participated in this project. My many conversations with Professor Rob Howe over the past three years have been central to the success of this ongoing project. Rob, I deeply appreciate the personal attention, the respect, and all of the encouragement you have given me as your student...even after I fried your multi-thousand dollar sensor in one of my very first experiments. I count it a great privilege to have had you as a role model during this time. Professor Sheridan, thank you for serving as a catalyst for this project especially in regards to the possible use of integrated robotic manipulators for image-guided cardiac surgery. Professor Rowell, having you as an advisor over the past year has proven extremely enjoyable

and very rewarding. Your expertise in image processing specific to guiding surgical procedures weighed into this body of work at a critical time. I will truly miss our Tuesday meetings which always promised an amusing anecdote or a great conversation about sailing or marathoning. Finally, to the engineers at Philips Medical Systems-thank you for your time and support at every stage in this project. In particular, Dr. Salgo and Bernie Savord, I wish you continued success as you pursue this exciting work with the rest of the BRP team.

These studies were supported by my wife Jane; my student and post-doc colleagues, especially Jeff, Doug, Pete, Paul, Amy, Yeong, Meena, and Ingeborg; and by a few grants (NIH F32-HL68404; Research Development Grant, Children's Hospital Boston; and Research Assistantship, MIT Department of Mechanical Engineering). Always remember that "They can make it harder but they can't make it longer" (unless you're a PhD student, of course). Aim High.

Table of Contents

List of Figures

List of Tables

Notational Conventions

Abbreviations

Heart Structures and Cardiac Surgery

AO	Aorta
ASD	Atrial Septal Defect
AV	Aortic Valve
CABG	Coronary Artery Bypass Graft
CHF	Congestive Heart Failure
CPB	Cardiopulmonary Bypass
EKG	Electrocardiogram
IVC	Inferior Vena Cava
IVS	Inter-ventricular Septum
LA	Left Atrium
LV	Left Ventricle
MV	Mitral Valve
MVA	Mitral Valve Annuloplasty
PA	Pulmonary Artery
PV	Pulmonic Valve
RA	Right Atrium
RV	Right Ventricle
SVC	Superior Vena Cava
TV	Tricuspid Valve

General

CT	Computed Tomography
EM	Electromagnetic
MRI	Magnetic Resonance Imaging
RMS	Root Mean Square
SEM	Standard Error of the Mean
TEE	Trans-esophageal Echo
US	Ultrasound

1 Introduction

ADVANCES in medical imaging have encouraged the development of new approaches to disease treatment in nearly every medical field. The conceptualization and implementation of so-called "image-guided surgery" draws on the expertise of a diverse group of engineers and medical subspecialists with two common goals: 1) make current procedures less invasive and thus less damaging to the patient and 2) develop new procedures for treating diseases which would not otherwise be possible without the use of medical imaging. The medical disciplines which have actively embraced this therapeutic revolution include such diverse fields as neurosurgery, gastroenterology, urology, and general surgery. Similarly, the imaging modalities employed for these procedures range from X-ray based techniques such as fluoroscopy and computed tomography (CT) to non-irradiating modalities like magnetic resonance imaging (MRI) and ultrasound (US).

Despite these advances, the one medical field with the most invasive treatment approaches available in modern medicine has not yet benefited from this revolution: cardiac surgery. In general, these procedures still require division of the breastbone, bypassing the bloodstream, and in some cases, arresting all circulation so that the surgeon can work either on the surface or deep inside the heart. This introductory chapter explains the conventional approaches to heart surgery in some detail as a preview to the challenges facing those who hope to make these procedures less invasive by using image guidance. Then, a brief review of recent applications of medical imaging as an interventional tool is provided. An overview of this thesis which addresses several of the challenges for developing image-guided cardiac surgical procedures then concludes this chapter.

1.1 Overview of Cardiac Surgery

As illustrated in Figure 1.1, the heart consists of an atrial chamber and a ventricular chamber on the left and right side which serve to pump blood through two parallel circuits in the body. The right side brings oxygen-poor blood from the body to the lungs while the left side pumps the oxygen rich blood from the lungs back into the rest of the body. Like all other organs in the body, the heart itself requires oxygen to function properly. Thus, the primary modes of heart disease requiring surgical intervention include inadequate oxygen delivery to the heart muscle or inappropriate function of one or more of the internal heart structures. Thus, modern cardiac surgery involves both procedures on the surface of the heart to improve oxygen delivery through coronary artery bypass graft (CABG) procedures as well as many types of surgical procedures inside the heart classified broadly as intracardiac surgery. This thesis focuses solely on the latter types of procedures as image-guided interventions have the most direct applications to procedures performed inside the heart.

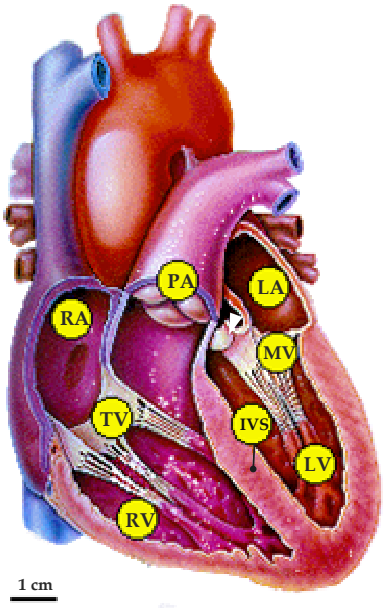

Figure 1.1 Normal anatomy of the human heart. RA=right atrium; PA=pulmonary artery; LA=left atrium; MV=mitral valve; IVS=inter-ventricular septum; LV=left ventricle; RV=right ventricle; TV=tricuspid valve; RA=right atrium. The aortic valve is marked with an arrowhead. Modified with permission from [1].

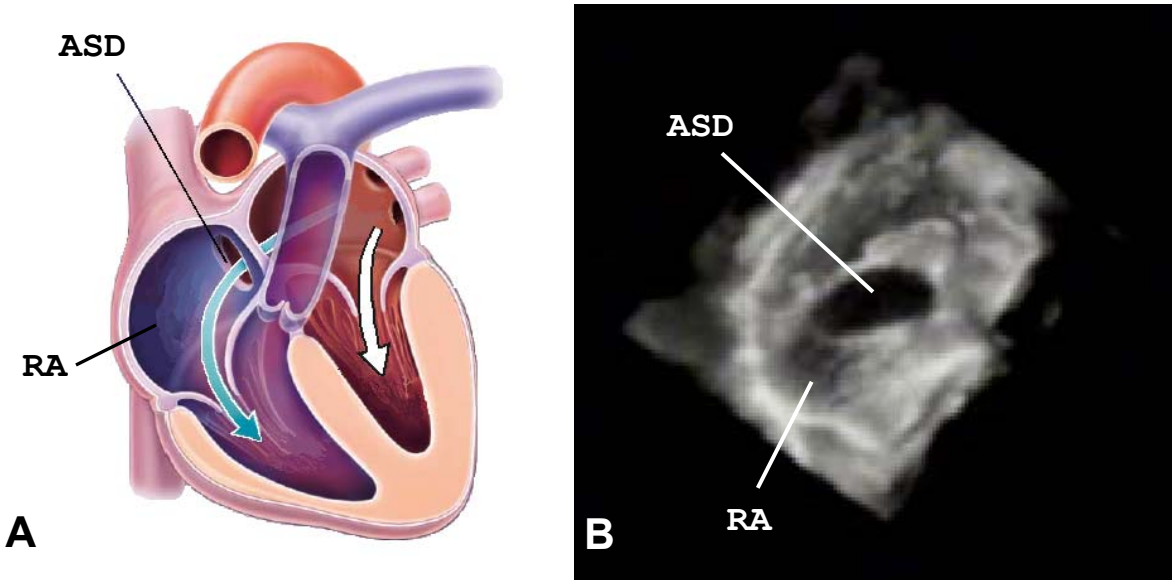

Figure 1.2 A) Illustration of an atrial septal defect (ASD) showing the normal direction of blood flow (white arrow) along with shunting through the defect. Modified with permission from [2]. B) 3-D US image of a large defect in the middle of the septum.

1.1.1 Intracardiac Surgery

True "open heart surgery" is usually performed to repair an internal defect or to repair or replace one or more of the heart valves. Figure 1.2 illustrates a heart defect in the atrial septum (ASD) along with a 3-D ultrasound (US) image of such a defect. Treatment options currently include catheter-based closure devices which can be used in a subset of patients with ASDs. Unfortunately, these devices have been hampered by mechanical failure, incomplete defect closure, and dislodgement. For most defects which are not centered in the septum and which come close to the specialized conduction tissue of the heart, surgical repair is performed.

Closure of atrial septal defects frequently requires use of a patch made of pericardium or synthetic material to cover the defect. The patch is fixed to the edge of the defect usually with sutures, taking care to approximate the patch and defect edge tightly to prevent residual holes. This type of repair is performed through conventional open heart surgery requiring both cardiopulmonary bypass and induction of cardiac standstill (fibrillation or arrest) so that the procedure is performed inside a relaxed heart. After the defect is closed, the surgeon closes the access incision in the heart while removing all air from the heart chambers (to prevent a stroke). Cardiopulmonary bypass is then discontinued as the heart begins to beat again. Recently, these procedures have been performed using small chest incisions and with robotic instruments [3-5]. Unfortunately, all of these surgical approaches still require

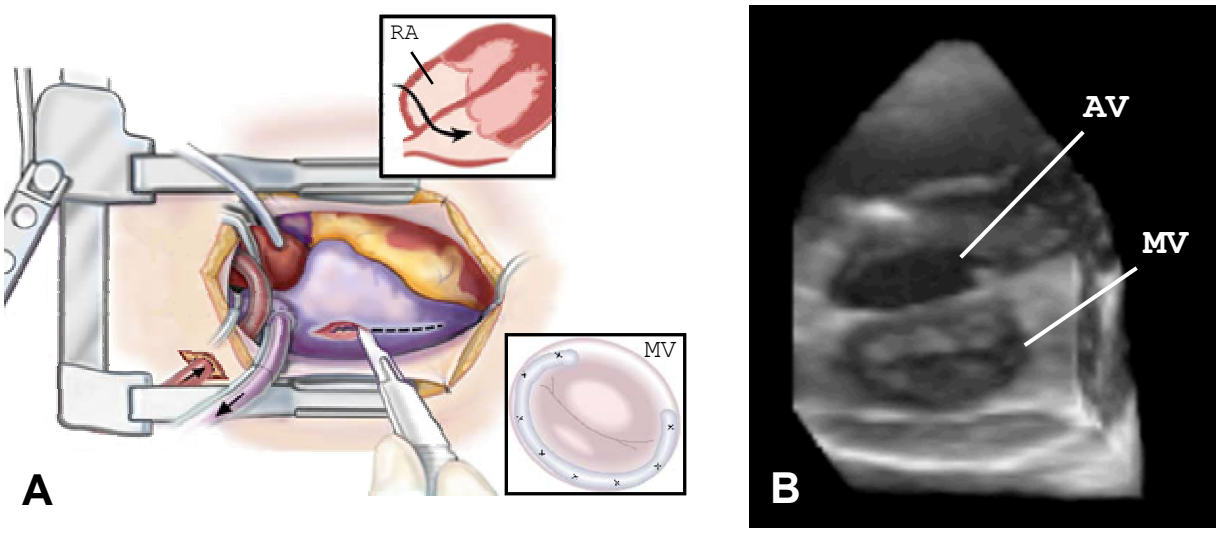

Figure 1.3 A) Mitral Valve Annuloplasty (MVA) with a supporting ring with access through the right atrium and atrial septum to reach the mitral valve (black arrow, top inset). The surgeon anchors a supporting ring to the outer portion of the valve with sutures (bottom inset). Note the CPB tubing which permits the surgeon works inside an empty and relaxed heart. Modified with permission from [6]. B) Real time 3-D US image of the mitral valve (MV).

cardiopulmonary bypass which carries significant risks for pediatric and adult patients alike as discussed later in this section.

Another common procedure performed inside the heart which might be amenable completion under image guidance is repair of the mitral valve (Figure 1.3). The mitral valve represents one of the most important structures inside the heart because it ensures unidirectional blood flow from the lungs into the body. When it becomes either narrowed or incompetent, patients experience severe and often debilitating symptoms ranging from congestive heart failure (CHF) to irregular heart rhythms. One of the main disease processes in the mitral valve is either progressive or acute dilation of the valve, with or without defects in the leaflets or supporting chordae, which makes the valve incompetent. Early surgical intervention in these cases before the ventricle begins to fail can improve patient outcomes. Today, when the mitral valve is dilated, up to 90% of these valves are spared with either mitral valve annuloplasty (MVA) or repair plus MVA which restores functionality without requiring valve replacement.

Just as with ASD closure, MVA uniformly requires conventional open heart surgery with CPB. The sequence of steps for performing these repairs parallels ASD closure. Similarly, recent attempts have been made to reduce the invasiveness of these procedures [7] including the use of minimally invasive robotic instruments [8]. However, all of these new approaches still require cardiopulmonary bypass with the procedure performed on an arrested heart. In addition to the problems with

cardiopulmonary bypass, in these patients, the surgeon has no way of assessing the quality of the repair until after the heart has been re-started and cardiopulmonary bypass discontinued. Thus, performing a surgical repair on a beating heart using image guidance would allow the patient to avoid cardiopulmonary bypass while the surgeon could assess the quality of the repair during the procedure.

1.1.2 Cardiopulmonary Bypass

For the past forty years, virtually all cardiac surgical procedures have been performed with the assistance of cardiopulmonary bypass. Developed in the early 1950's, this technology revolutionized the practice of cardiac surgery by enabling both CABG procedures and a broad spectrum of intracardiac procedures [9]. Figure 1.4 shows a small child placed on cardiopulmonary bypass which perfuses the patient's body with oxygen-rich blood so that the surgeon can work inside a relaxed heart. In addition to most CABG procedures, cardiac surgeons in the United States rely on cardiopulmonary bypass to repair 20,000 congenital cardiac anomalies and to perform 10,000 adult valve procedures each year for a total of over 330,000 procedures every year [10].

Although cardiopulmonary bypass plays a central role in most cardiac surgical procedures, many recent studies indicate significant risks associated with this process. As Table 1.1 shows, these risks can be divided into hematologic (blood-borne) risks, mechanical risks, and general multi-factorial

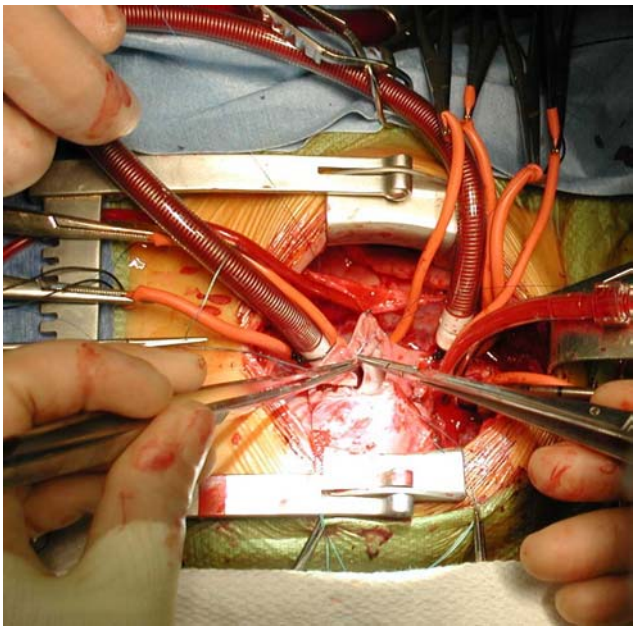

Figure 1.4 Open heart surgery to repair a septal defect in a small child. The large red (blood-filled) tubing is connected to an external cardiopulmonary bypass machine so that the surgeon can work inside a relaxed heart.

Table 1.1 Risks of Cardiopulmonary Bypass

SIDE-EFFECT	COMMENT	REFERENCES
Hematologic		
Activation of Complement	C3a, prekallekrein, XIIa; IL-6 & -8 and TNF-1 & -2 elevated. Some linked to neurodevelopmental delay in children	[11-14]
Increased Inflammatory Mediators		
Mechanical		
Microemboli	Particulate matter from aortic cross-clamping; small to large air bubbles from inserting bypass tubing, or from the bypass pump. Number of emboli correlated to neuropsychiatric dysfunction	[10, 15, 16]
Air Embolus		
Multifactorial		
Multi-organ dysfunction	Increased risk with other co-morbidities	[17, 18]
Death		

risks. Hematologic risks arise primarily from the blood contacting the foreign surfaces of the bypass tubing and the other elements of the pump circuit. Mechanical risks relate to the process of inserting tubing into the heart and the major vessels and to mechanical problems with the bypass circuit. Finally, the multifactorial risks have been noted with increased frequency in patients undergoing bypass but have not been attributed to one specific etiologic cause. Thus, cardiopulmonary bypass has allowed surgeons to operate on many diseases which previously had no cure, but the associated risks merit attempts to perform these procedures without using cardiopulmonary bypass if at all possible.

1.1.3 Beating Heart Surgery

The first cardiac surgical procedures were accomplished prior to the development of cardiopulmonary bypass. Following Harken's pioneering work during World War II, several surgeons attempted and subsequently established a number of procedures ranging from finger fracture of calcified mitral valves [19, 20] to use of a rubber "well" to repair septal defects [21] and introduction of a cardioscope for guiding intracardiac repairs. These truly open heart procedures place patients at high risk for air and particulate emboli as well as massive blood loss. In addition, inadequate visualization led to high recurrence rates. However, until the development of cardiopulmonary bypass, there was no other treatment for these diseases.

In the mid-1950's, these pioneers of beating heart largely abandoned their efforts as cardiopulmonary bypass became safer and more readily available [22]. However, the great risks of cardiopulmonary bypass enumerated above and recent advances in instrumentation have motivated surgeons to develop new, safer methods for operating on the heart without bypass. Early results of "off-pump" CABG procedures on the surface of the heart appear promising [23, 24].

Understandably, attempts to perform procedures inside the heart have been much more limited due to the inability to visualize internal heart structures through blood. One investigator noted extreme difficulty in repairing an internal heart defect using a modified optical endoscope [25]. Another investigator recently noted similar difficulty using 2-D ultrasound (US) imaging for guiding heart valve repairs [26]. However, a recent report shows many of these problems can be overcome by using 3-D volumetric US imaging to guide procedures inside the heart [27]. This thesis summarizes on our similar experience using real time 3-D US imaging to guide internal heart procedures without using cardiopulmonary bypass.

1.2 Recent History of Image-guided Interventions

Inadequate visualization represents the principal obstacle to performing robust repairs of heart defects and valve abnormalities inside the beating heart. As illustrated by the recent success of CABG procedures performed without bypass, if the surgical site can be adequately visualized, instruments can be tailored to enable the surgeon to perform the necessary steps to complete the procedure. As illustrated above, because blood is opaque, optical imaging inside a beating heart proves inadequate. Thus, any surgical procedure performed inside a beating heart will inherently be "image-guided." Consequently, this work focuses on medical imaging capable of visualizing the internal structures of the blood-filled heart. The following paragraphs review lessons learned from other fields of image-guided surgery and then specifically focus on the two candidate imaging modalities guiding cardiac surgery: MRI and US.

1.2.1 Imaging Modalities

As reviewed in [28, 29], the number of procedures guided by some form of imaging is rapidly increasing along with the sophistication of the imaging modalities used for these interventions. Since the discovery of X-rays in 1895, images have been used to guide therapy beginning with the removal of a bullet from the leg of a gunshot victim [30]. Today, many different medical imaging modalities are used to guide procedures including x-ray angiography and fluoroscopy, CT, MRI, and US.

The imaging techniques which permit real time visualization of the interventional process include x-ray angiography and US. In addition, recently developed "open" MRI systems offer "nearly real time" imaging for guiding interventions [31]. In this process, the surgeon, radiologist, or cardiologist performs some intervention such as insertion of a needle into the body while viewing the internal part of the procedure on a CRT or LCD monitor. This process should be distinguished from laparoscopic or endoscopic procedures where a direct optical image of the process is viewed using a medical grade CCD camera. In the case of image-guided interventions, the process at the tool tip is obscured from view so the physician has only the image on the display to inform the next maneuver. Thus, the quality of the image can directly affect the success or failure of the procedure. Consequently, multi-modal imaging is becoming a common trend in image-guided surgery so that the strengths of each imaging modality can be combined to overcome any inherent shortcomings.

The strengths and weaknesses of some of the most common interventional imaging modalities are summarized in Table 1.2. For cardiovascular procedures, the possible modes include X-ray angiography, cardiac MRI, and US. X-ray angiography requires intravenous contrast to visualize soft tissue boundaries and sometimes involves significant radiation exposure especially when multiple procedures are required over time. Thus, this modality does not represent a viable choice for visualizing intracardiac procedures. Recently, MRI has proven useful for guiding intracardiac manipulations. With increased computer processor speed, "MRI fluoroscopy" has an image refresh rate of five to eight frames per second which proved sufficient for guiding a catheter in a recent study [32]. However, MRI for interventional procedures involves tremendous overhead for the initial setup from anesthesia equipment to surgical instrumentation which must be either attached to long cables and tubing or made of nonparamagnetic materials. In addition, the open MRI systems in which these procedures are performed have much less resolution than conventional long-bore, high field intensity imaging magnets [31]. As described below, real time 3-D US can overcome many of these limitations for guiding surgical procedures.

1.2.2 Techniques for US-guided interventions

Ultrasound offers advantages of good soft tissue resolution, portability, and applicability in a wide range of clinical settings with minimal expense [33, 34]. Ultrasound has also been used to guide a variety of interventional procedures including tumor biopsy and abscess drainage [35] with very few procedure-related complications [36]. However, 2-D US imaging gives only a cross-section view of the procedure with no out-of-plane information. Thus, the only procedures that can be effectively guided by 2-D US are those where a rigid tool such as a biopsy needle can be held in the plane of the image as it is advanced towards the target [33, 37].

Table 1.2 Characteristics of Imaging Modalities Used for Image-Guided Surgery

MODALITY	STRENGTHS	WEAKNESSES	COMMENT
X-ray Fluoroscopy	Real time (30 fps) Good bone contrast	Radiation exposure Little soft tissue contrast	Primarily for orthopedic procedures
X-ray Angiography	Real time Visualizes cavity boundaries well	Radiation exposure Contrast injection required	Used for visualization of vascular structures or the bile ducts
CT	Good contrast for many soft and bony tissues High quality 3-D reconstruction (offline)	Radiation exposure Not real time	Can guide drainage procedures (e.g. cysts) and biopsy with intermittent imaging
MRI	Good contrast for most soft tissues Functional studies also possible	Open MRI for "nearly real time" expensive Special equipment required	Neurosurgery, breast tumor resection, spine surgery, among others
2-D US	Good oft tissue contrast Portable No adverse effects	No spatial orientation Poor signal to noise ratio	Primarily for guiding a rigid needle that can be held in the image plane.
3-D US	Now 20-25 volumes per second	Limited spatial orientation Poor signal to noise ratio	New modality for interventions

To expand the number of clinical applications for US-guided interventional procedures, investigators have used several approaches to overcome the limitations inherent in 2-D imaging. These include integration of 2-D US images into a 3-D augmented reality operative scene [38] and use of a robotic arm for computer-assisted positioning of a biopsy needle under US guidance [39, 40]. Unfortunately, these approaches require additional equipment which detracts from the flexibility, portability, and reduced expense which US imaging offers over CT or MRI-guided interventions.

Surgeon-controlled US (i.e. ultrasound imaging performed by the surgeon rather than by a sonographer) has become increasingly popular and represents another possible approach to overcoming the limitations of 2-D US for guiding interventions [41, 42]. Theoretically, navigational accuracy is enhanced by improving the surgeon's intuition for the alignment of the surgical tool with the operative target displayed in the US image [43]. However, the advantages of surgeon-controlled interventional US have not been conclusively demonstrated.

Three-dimensional US imaging has great potential for interventional applications [44, 45]. However, acquiring and rendering 3-D US images with the resolution and frame rate required for guiding procedures has proven quite challenging [45-48]. Most 3-D US systems combine specialized acquisition methods with off-line image processing to produce a 3-D image. Consequently, although these imaging techniques may offer additional spatial orientation information, until the very recent introduction of real time 3-D US, time lags have limited applications for this imaging modality to diagnosis [49, 50] and surgical planning [51].

1.3 Thesis Summary and Organization

This thesis is divided into four additional chapters. Following this introductory chapter, the next three chapters discuss in detail the specific work performed by the author for this thesis. The final chapter summarizes the contributions and offers suggestions for future research efforts in this field. The three chapters with new contributions include the following.

Chapter 2. Feasibility of Beating Heart Intracardiac Surgery Using Real Time 3-D Ultrasound

In this chapter, the use of real time 3-D US images for guiding surgical tasks is reported. Specifically, the development of an animal model for studying this new approach to image guided interventions is detailed. Findings from these initial studies identified some important limitations to the current imaging setup which motivated subsequent investigations. These limitations included lack of safety measures to prevent inadvertent injuries during beating heart intracardiac procedures and difficulties navigating the surgical instruments back into the US field of view at the beginning of the procedure and following any subsequent excursions out of view.

In addition, an *in vitro* tank study was designed in which seven surgeon subjects performed surgical tasks using a range of imaging techniques including real time 3-D US. This study permitted comparison of this imaging modality with 2-D US and with endoscopic imaging. Techniques such as altering the 3-D view of the surgical field and having the surgeon hold the imaging probe were also explored.

Chapter 3. Segmentation Techniques for Real Time Volumetric Ultrasound

Manipulating the image data taken from the real time 3-D US system represents a fundamental step towards enabling image guided procedures using this modality. In this chapter, segmentation schemes are reviewed with a particular focus on manual and semi-automatic segmentation of medical

images. A new active contour algorithm recently reported in [52, 53] is briefly presented as this segmentation technique has performance characteristics which are very favorable for use with real time 3-D US including good computational efficiency and accuracy. Software tools developed by the author for performing both manual and semi-automatic segmentation on US volumes are demonstrated. Finally, a specific application for the semi-automatic segmentation algorithm for improving the safety of US-guided procedure in the form of "virtual fixtures" is presented.

Chapter 4. Atlas-based Model Matching as a Navigational Aid

Some of the early animal procedures performed in this work combined US imaging with EM instrument tracking. As part of the instrument tracking system, a graphical model of the heart registered to the animal's actual heart was displayed with the instrument tip animated within this model. In these studies, the problem of navigating the instrument into the US image was completely eliminated with improved procedure efficiency and safety. Thus, in this chapter, an integrated approach to registering a graphical model of the heart to the patient's anatomic landmarks is presented as a navigational aid for US-guided interventions. This process requires spatial compounding of multiple US volumes to encompass the relevant internal heart landmarks in a single image volume. Then, control point pairs are identified both in the composite US image and on a graphical model derived from the Virtual Human Project. The transform matrix inferred by these control point pairs is determined and applied to the heart model to complete the registration process. The fit between the US images and the heart model is then evaluated.

Introduction

2 Feasibility of Beating Heart Intracardiac Surgery Using Real Time 3-D Ultrasound

PRELIMINARY research efforts to enable image guided surgery in a beating heart without the use of cardiopulmonary bypass include development of an animal model for these procedures and further testing using an *in vitro* setup inside an acoustic imaging tank. Procedures performed on the animal model gave specific insights into the possible procedures which could be performed using this imaging modality as well several important limitations. In addition, an *in vitro* tank study involving seven surgeon subjects permitted the further evaluation of the potential uses for real time 3-D US for guiding surgical procedures. In this study, specific parameters facilitated the quantification of performance using real time 3-D US vs. 2-D US vs. optical imaging. Instrument tracking gave further insights into the specific differences between these imaging modalities. Furthermore, input from each subject served to guide further investigations detailed in subsequent chapters in this thesis.

2.1 Imaging System

The imaging system used for the studies presented in this thesis (LIVE 3-D ECHO) was recently released by Philips Medical Systems Ultrasound Division (Andover, MA). Additional technical and engineering support was offered by Philips for these studies as part of a larger multi-institution collaborative research agreement. The US system consists of a hand-held transducer (xMATRIX™) and an image processing platform (xSTREAM). The imaging probe (Figure 2.1A) contains approximately 3,000 active piezoelectric crystal elements arranged in a fully-sampled 2-D array operating in a broadband 2-4 MHz range. Initial tank studies have shown a lateral resolution of 1.7±0.4 mm when used to image 4 mm diameter glass beads at a distance of 10 cm.

The image processing and rendering platform is based on a dual 2.2 GHz Pentium 4 processor PC which supports multiple imaging modalities including conventional B-mode 2-D US, 2-D color flow Doppler imaging, biplanar 2-D US (i.e. orthogonal 2-D images displayed side-by-side), and several real time volume rendered modes. These volume rendered modes are based on traditional ray-casting methods where the opacities encountered by each sonographic "ray" are blended to yield the opacity of an individual pixel, $P(r)$ given by Equation (2.1):

$$P(r) = \sum_{k=0}^{K} [c(r,k)\alpha(r,k) \prod_{i=k+1}^{K} (1-\alpha(r,i))] \tag{2.1}$$

where $c(r,k)$ is the shade value and $\alpha(r,k)$ is the opacity value for each k^{th} voxel along the r^{th} ray [54].

In the volumetric real time mode, this system can render 20-25 volumes per second consisting of 128x48x208 voxels each. (Throughout this thesis, US volumes are given as L_1xL_2xA where L_i are the lateral directions and A is the axial direction along the direction of US wave propagation.) The image

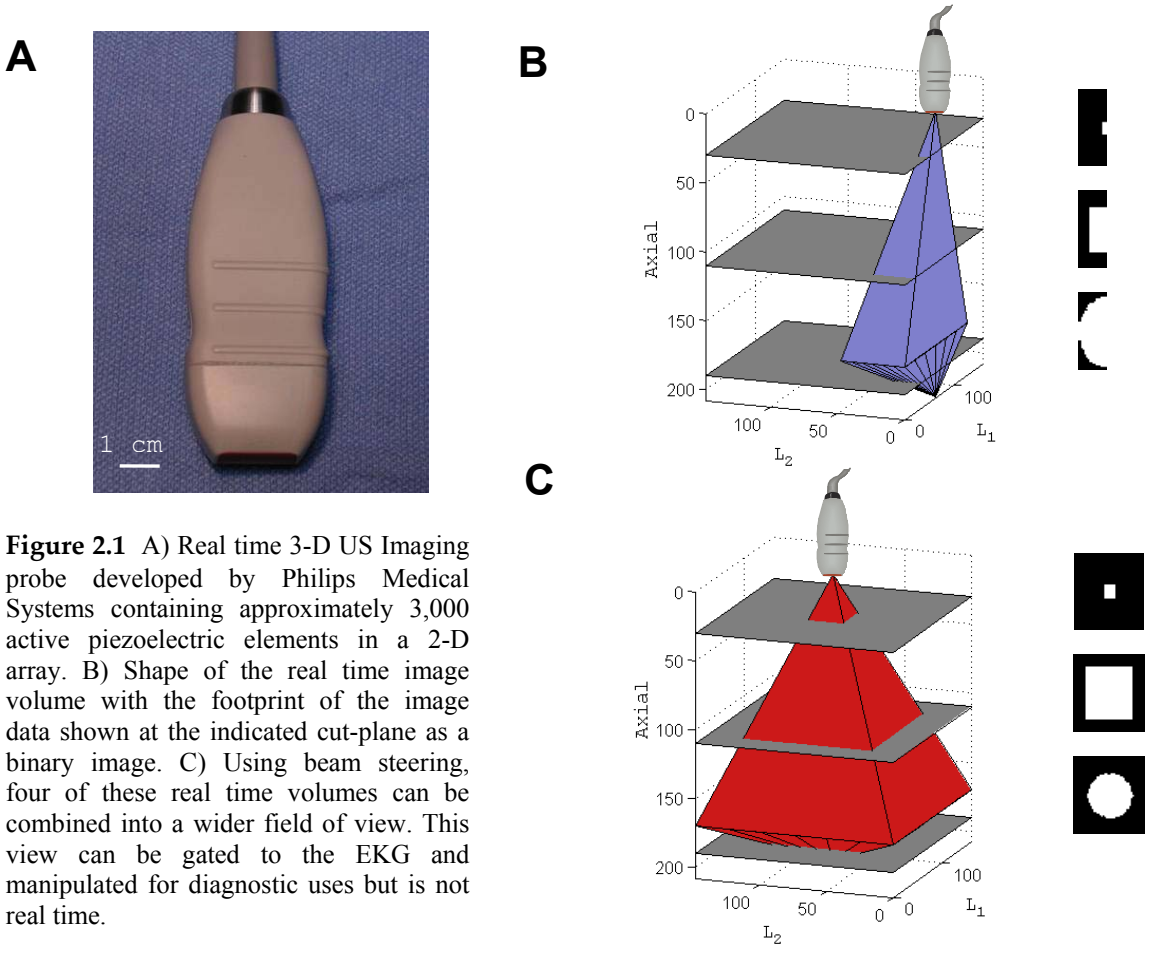

Figure 2.1 A) Real time 3-D US Imaging probe developed by Philips Medical Systems containing approximately 3,000 active piezoelectric elements in a 2-D array. B) Shape of the real time image volume with the footprint of the image data shown at the indicated cut-plane as a binary image. C) Using beam steering, four of these real time volumes can be combined into a wider field of view. This view can be gated to the EKG and manipulated for diagnostic uses but is not real time.

footprint within this volume is shown as a binary image in Figure 2.1B. Another volumetric imaging mode termed "full volume mode" uses beam steering to assemble four of these smaller "real time" volumes into a larger composite image of 160x144x208 voxels (Figure 2.1C). This mode is not real time but allows the user to examine a larger region of interest offline. The system used for these studies permits the user to download both the real time and full volume images as post-scan converted gridded data sets. The results presented in Chapters 3 and 4 were obtained in this manner.

2.2 *In vivo* Model for Understanding Beating Heart Surgery

To better understand the challenges unique to performing surgery inside a beating heart with US imaging as the only means of visualization, we performed a series of large animal procedures. The primary goal of these studies was to learn how to safely place instruments inside the beating heart and then move them around the heart chambers performing basic surgical tasks. This involved determining the appropriate approach for the surgical instruments, proper positioning of the imaging probe, and ensuring the procedure proceeded safely and efficiently. This section details these experiments and the lessons learned which motivated the research detailed in Chapters 3 and 4.

2.2.1 Surgical Setup

As outlined in Chapter 1, repair of atrial septal defects (ASDs) is a common intracardiac procedure which would ideally be performed without cardiopulmonary bypass. Thus, the animal model we developed for this study involved creating a defect in the atrial septum which can then be repaired. For this study, we chose to use Yorkshire pigs due to their ready availability and their general good tolerance of anesthesia. Because the common atrial septum in swine is relatively small, creating a septal defect under US guidance would permit us to identify the major challenges for performing more complex surgical maneuvers in the future.

All procedures were performed in accordance with NIH guidelines on the humane treatment of animals with the approval of the Animal Care and Use Committee, Children's Hospital Boston. For these procedures, a 15-30 kg pig is placed under general anesthesia. A large intravenous catheter and an arterial pressure line are then placed in the femoral vessels. A full chest incision (sternotomy) is made to give ready access to the heart surface. Although these initial procedures are performed with an open chest, our goal is to eventually progress to a closed-chest approach for these procedures. Following the sternotomy, the incision is extended into the fourth rib space, and the right lung is packed out of the surgical field. The pericardium is then anchored to the chest wall to keep the heart in the midline.

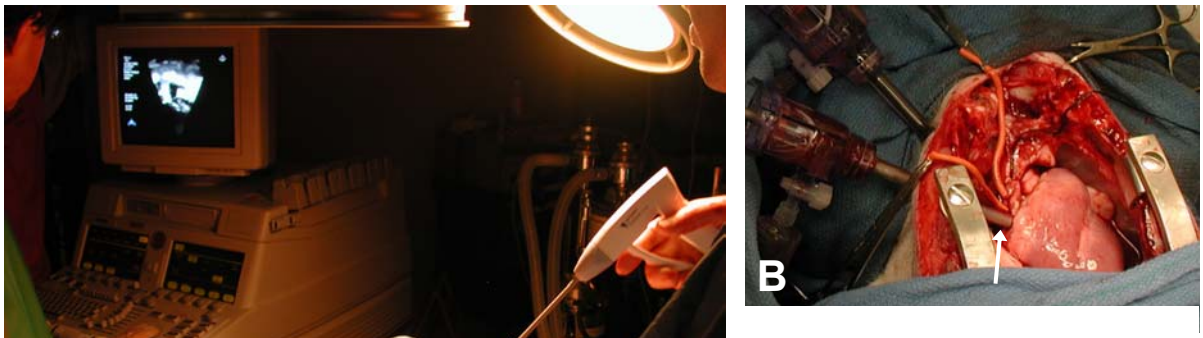

Figure 2.2 A) Surgical setup showing the surgeon (right) facing the US system while manipulating an instrument. The sonographer (left) places the probe directly on the heart for optimal image quality. B) Detail of the surgical setup showing two trans-atrial instrument ports (arrow).

Once the heart is exposed, an atrial purse string suture is placed in the right atrial appendage. Then, a custom 7 mm port is placed through the atrial purse string. This hollow port is filled with heparinized saline to prevent air entrainment with instrument insertion while blood loss is minimized by a gasket mechanism. The port is then secured within the atrial wall by cinching up on the circular suture around the port. This port permits access to the intracardiac structures with thoracoscopic instruments. Figure 2.2 shows the overall setup as well as a detail of the port placement into the right atrium for ASD creation.

After safely obtaining port access to the atrial chamber, the surgeon then slowly advances the instrument until the tip appears inside the US image. Once the instrument tip is visualized, the surgeon and the sonographer work together to guide the tip to the target. In these cases, the target is the common atrial septum located posterior to the back wall of the aorta. The surgeon advances the instrument until it contacts the septal wall. When contact is confirmed by the sonographer and the instrument is seen to be well below the aorta and aimed toward the left atrium, a sharp blade is advanced out of the instrument tip and the instrument is then advanced further until the tough, fibrous septum has been penetrated. The instrument is then withdrawn, and the sonographer images the septum with both 3-D US and color-flow Doppler to confirm the presence of a defect and to measure its size. In addition to this simple task, other navigational tasks to various intracardiac structures were performed. In these instances, the surgeon navigates to a given landmark and then deploys a small helical metal tack into the target tissue.

2.2.2 Navigational Techniques

In these procedures, we used both 2-D and 3-D US imaging for guidance both with and without the assistance of electromagnetic (EM) tracking equipment for a total of four study groups: 2-D US guidance alone (n=5); 3-D US guidance alone (n=3); 2-D US guidance + EM tracking (n=2); and 3-D US guidance + EM tracking (n=1). All procedures were performed by the author with US imaging performed by Dr. Jerry Marx and EM mapping performed by Dr. John Triedman both at Children's Hospital Boston. The order of these procedures varied randomly because of equipment availability thus eliminating any learning bias.

Optimal positioning of the US probe had not previously been described. Although 2-D imaging is possible using a trans-esophageal (TEE) probe behind the heart, this type of probe has not been developed for real time 3-D imaging. Thus we studied three different positions for placing a hand-held probe during these procedures: sub-xyphoid, sub-diaphragmatic, and direct epicardial. This analysis was performed during the first two animal procedures to determine optimal positioning for the remaining procedures.

The electromagnetic tracking portions of this study will be described in detail in Chapter 4. Briefly, the CARTO electromagnetic mapping and tracking system (Biosense Webster, Diamond Bar, CA) consists of three transmitters and a catheter-based sensor which can both create a graphical map of the heart chambers and display the position of the catheter within this map. This system has reduced operator dependence on fluoroscopy for intracardiac navigation during arrhythmia ablation procedures [55-57]. In the experiments presented here, a graphical map of the animal's right atrium was created using the CARTO catheter at the beginning of the procedure. The same mapping catheter was then fixed to the surgical instrument and inserted into the heart chamber with the instrument so that the instrument tip could be accurately tracked. Thus, in the procedures with US navigation plus tracking, the surgeon has a method of navigating the tool into the US field of view and then two independent means of navigating to the surgical target.

2.2.3 Results

In the initial experiments, images obtained from the sub-xyphoid position were of poor quality with significant artifacts. From the sub-diaphragmatic position, image quality improved, but this approach required flooding of the chest cavity with fluid to clearly see the intracardiac structures and to track intra-atrial instruments. Placing the US probe in an off-axis direct epicardial position (just to the right of the IVS) gave high–quality images of the septum and both atria with minimal image artifact from

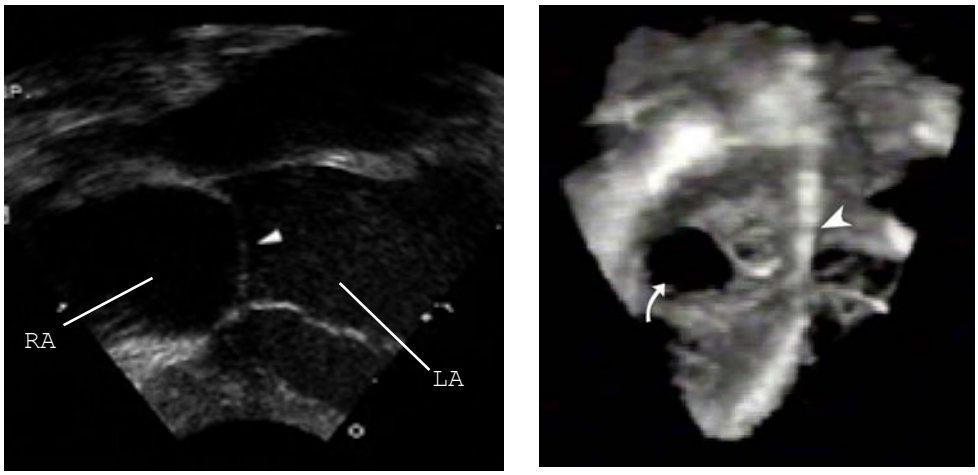

Figure 2.3 2-D (left) and 3-D (right) US images of the atrial septum (arrowhead) obtained from a direct epicardial imaging approach. White arrow in the 3-D image=SVC inlet.

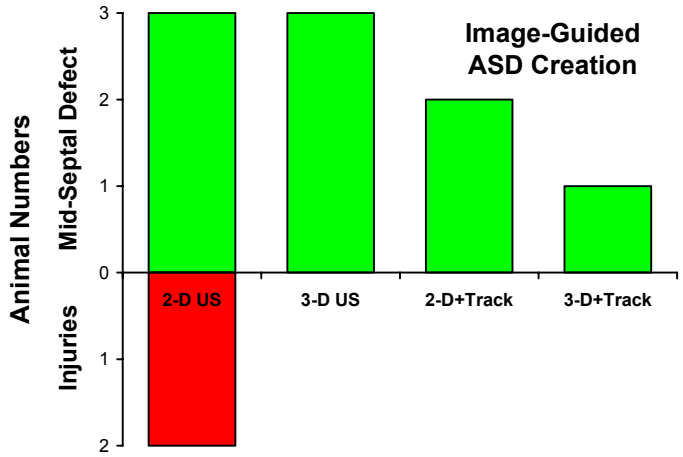

Figure 2.4 Summary of procedure outcomes for all approaches to image-guided trans-atrial intracardiac procedures in a beating heart. These include 2-D US alone, real time 3-D US, and US with electromagnetic instrument tracking. In the latter three groups, no inadvertent injuries have occurred.

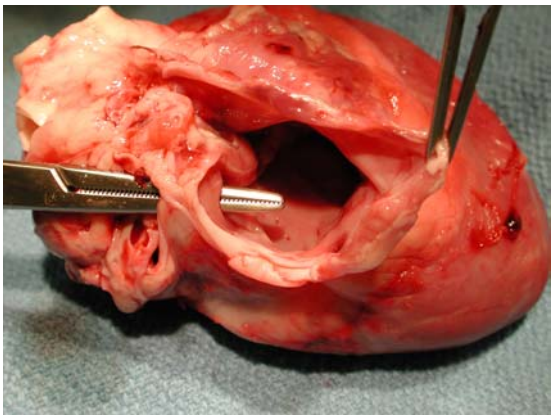

Figure 2.5 Successful creation of a mid-septal ASD using 3-D US guidance + EM tool tracking. This view is through the posterior wall of the right atrium with the superior and inferior vena cava divided.

intracardiac instruments and no interference between the surgeon and the sonographer. Examples of both 2-D and 3-D epicardial images are shown in Figure 2.3.

Navigation to the atrial septum and safe creation of an ASD proved very difficult with 2-D US guidance alone. Out of five attempts, two resulted in serious inadvertent injuries leading to the early demise of the animal. One injury was to the posterior wall of the aorta and the other to the posterior wall of the atrial chamber. Furthermore, navigating the instruments into position also proved quite challenging as only a cross-section of the instrument is seen even when the tool is within the imaging plane. With real time 3-D US or with the addition of the graphical map and instrument tracking, ASD creation was performed safely in all six animals. These results are summarized in Figure 2.4 with an example of a mid-septal ASD created using these techniques shown in Figure 2.5.

2.2.4 Discussion

This series of eleven procedures represent the first known attempt to perform surgical procedures inside the beating heart using real time 3-D US in the United States. The results presented above also point very clearly to several areas for future work to ensure the safety of future procedures. Most notably, 2-D US alone proved entirely inadequate for guiding tasks inside the heart due to the inability to keep the surgical tool within the imaging plane. These procedures also showed the importance of establishing some type of additional safety measures to prevent inadvertent injuries. Although the position of the tool was confirmed as well as possible at all times, slight errors in positioning can have devastating consequences when working within such a small space.

The improved results achieved with using either real time 3-D US alone or the addition of the CARTO electromagnetic tracking device for navigational assistance underscored the importance of

understanding spatial relationships during image-guided procedures. The volumetric nature of the 3-D US image can sometimes resemble an endoscopic view of the surgical field by placing the image in the appropriate orientation and by occasionally moving the image to demonstrate the spatial relationships with in the image. However, the field of view of this image is much smaller than that of a conventional endoscope; thus, it proved very difficult to re-position the surgical instruments back into view if for any reason they strayed from the region of interest. The added orientation information provided by the CARTO system proved so useful that even 2-D-guided surgical procedures could be performed efficiently with no inadvertent injuries. When combined with 3-D US, the procedures were even more straightforward with less time spent searching for the instruments.

Downing and colleagues reported a similar experience using 2-D echo imaging to guide suturing of the mitral valve leaflets with 25% of sutures misplaced or snaring other structures [26]. Conversely, Sogawa, et al report the ability to suture inside the heart with good accuracy using real time 3-D imaging [25]. Thus, performing complex maneuvers during image guided surgery seems to require a 3-D image. To further evaluate this hypothesis, a carefully controlled surgical simulation study was then performed.

2.3 *In vitro* study for quantifying 3-D US-guided task performance

As shown above, 2-D US offers little spatial orientation information limiting its use for guiding complex surgical manipulations. On the other hand, high resolution real time 3-D US can potentially overcome this limitation thereby expanding the applications for interventional US. The following *in vitro* tank study examines the benefits of real time 3-D US for performing both basic and complex image-guided surgical tasks.

2.3.1 Methods

For this study, a custom tank was prepared for evaluating surgical task performance under simulated clinical image-guidance conditions. This tank consists of a plastic reservoir covered by an opaque dome through which surgical instruments are inserted. The bottom of the tank is lined with a layer of acoustic polymer (Sylgard 170, Essex Brownell, Edison, NJ) mixed with Ni powder (Atlantic Equipment Engineers, Bergenfield, NJ) and microballoons (Potters Industries Inc., Carlstadt, NJ) to minimize reflections. Degassed double de-ionized H_2O serves as the imaging medium inside the testing tank.

Seven surgical trainees with experience in minimally invasive endoscopic surgery were recruited for this study (average surgical training=4.6 years). Each subject performed three endoscopic surgical tasks inside the testing tank guided by endoscopic imaging, 2-D US, and 3-D US. In addition, biplanar 2-D US, surgeon-controlled US, and modified views of the 3-D images were also tested on one of the surgical tasks. After three practice attempts with each imaging modality, subjects performed the task under endoscope guidance which was used as a performance normalization factor for each subject. A Latin squares scheme was used to randomize the order of US image presentation to avoid learning bias in the task performance data set. All images aside from surgeon-controlled imaging were obtained by the same sonographer using appropriate interventional US imaging techniques [37]. As shown in Figure 2.6, the setup for this study closely resembled the surgical setup in the animal procedures described above.

Figure 2.6 Tank study setup. In this arrangement, the surgeon (white coat) cannot see the task inside the tank except by viewing the US image on the monitor.

Surgical Tasks

The three surgical tasks were Bead-in-Hole Navigation, Bead-to-Bead Navigation, and Clip Fixation (Figure 2.7). The first task required subjects to place a 4 mm diameter plastic bead into a 5 mm hole in a canvas sheet. Starting with a plastic bead in the jaws of a standard endoscopic grasper (Ethicon Endosurgery, Cincinnati, OH), the tool was positioned approximately 6 cm from the target hole on the perimeter of an oval frame suspended in the testing tank. With both the tool and target hole

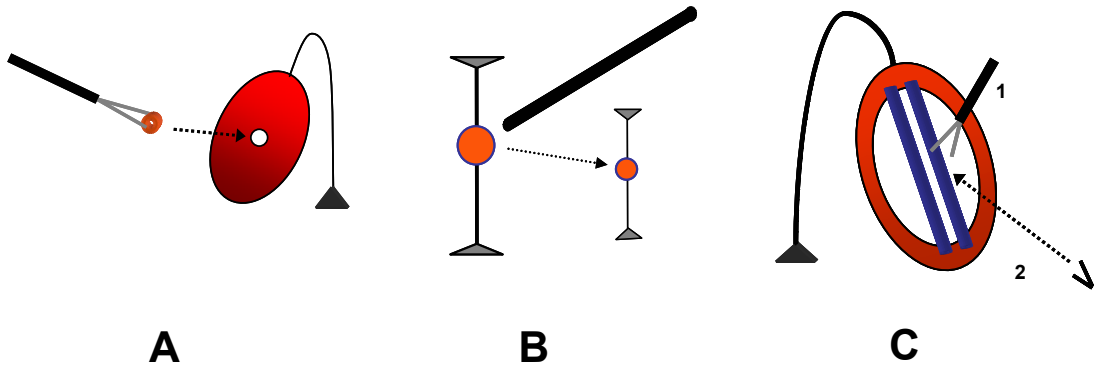

Figure 2.7 Illustrations of the three image-guided tasks. A) Bead-in-Hole Navigation; B) Bead-to-Bead Navigation; C) Clip Fixation which proceeds in two steps.

in view on the US system screen, subjects attempted to insert the bead through the hole. This task was used to demonstrate feasibility; thus, only endoscope, 2-D US, and 3-D US completion times were measured.

Bead-to-Bead Navigation tested the ability of subjects to navigate between two objects without any limitations on tool tip position. Two plastic beads were suspended inside the testing tank 6.3±0.3 cm apart, and a blunt surgical tool was used to navigate between them. All subjects started with the tool tip touching the bead closest to their dominant hand and then attempted to move the tool tip to the target bead as quickly and directly as possible. Subjects completed this task using 2-D US, biplanar 2-D US, 3-D US, and surgeon-controlled US (2-D and 3-D). In addition, modified 3-D views were evaluated. This modified 3-D presentation involved rotating the image "backwards" to give the operator a more horizontal view of the beads (15° view) or rotating the image "forward" to a more vertical perspective (75° view).

Finally, Clip Fixation is a common surgical maneuver used to anchor a repair patch in place or to fix adjacent tissues to one another during reconstructive surgery. Starting from a peripheral location on the task frame, subjects maneuvered a grasping tool and an endoscopic clipping tool (Ethicon Endosurgery) into the US field where two adjacent 5 mm diameter rubber tubes were held in view by the sonographer. Subjects then approximated the adjacent tubes with the grasper and fixed them together with a metal clip.

Performance Measures

Task performance measures were completion times (measured by an observer viewing the task through an endoscope), mean and maximum deviation from a straight-line path (Bead-to-Bead Navigation), and misapplied clips (Clip Fixation). Tool tip trajectories were measured with an electromagnetic tracking device (Flock of Birds, Ascension Technologies, Burlington, VT) fixed to the handle of the surgical instrument. Using the nomenclature of Figure 2.8, mean deviation, D_{mean}, and maximum deviation, $D_{\max}$, from a straight-line path were then calculated with the following equations:

$$D_{mean} = \frac{1}{n}\left(\sum_i h_i + \sum_j h_j \sin\theta_j + \sum_k h_k \right) \tag{2.2}$$

$$D_{\max} = \max_{i,j,k} \{h_i, h_j \sin\theta_j, h_k\} \tag{2.3}$$

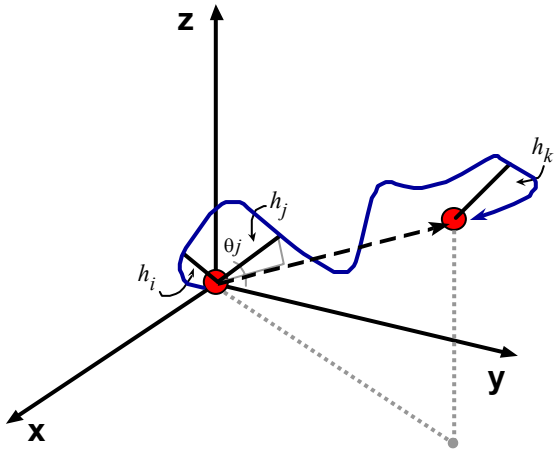

Figure 2.8 Coordinate frame for trajectory analysis. The blue line represents a typical tool tip path traveling from one bead at the origin to the target bead as shown.

Here h_i, $h_j \sin\theta_j$, and h_k represent minimum distance vectors from the straight-line path between the beads to each acquired data point along the tool tip path where the latter consists of n data points.

For Clip Fixation, the task was considered complete when a secure fixation clip had been applied across both tubes. Errors were defined as a clip applied incorrectly to a single tube thereby failing to successfully approximate the two tubes. In the event of a misapplied clip, subjects were instructed to continue attempts to approximate the tubes until the task was completed successfully.

Statistical Analysis

Comparisons of all task performance measures between US imaging modes were made using a paired one-tailed Wilcoxon signed rank test (SPSS 10.1, Chicago, IL). For all comparisons, $p \leq 0.05$ was considered statistically significant.

2.3.2 Results

As shown in Figure 2.9A, Completion times for Bead-in-Hole Navigation decreased by 50% using 3-D US vs. 2-D US guidance (p=0.046). For Bead-to-Bead Navigation (Figure 2.9B), normalized task completion times decreased by 77% with 3-D US guidance as compared to 2-D guidance (p=0.009). Trajectory analysis also demonstrated significant improvement in navigational accuracy using real time 3-D US as compared to 2-D US imaging. With 3-D US guidance, D_{mean} decreased from 1.62 cm to 0.87 cm (46% improvement, p=0.040) while $D_{\max}$ decreased from 3.55 cm to 2.12 cm (40% improvement, p=0.069). (For reference, D_{mean} and $D_{\max}$ with endoscope guidance were 0.30±0.04 cm and 0.92±0.18 cm, respectively.) Example trajectories for 2-D and 3-D US-guided navigation for this task are shown in Figure 2.10.

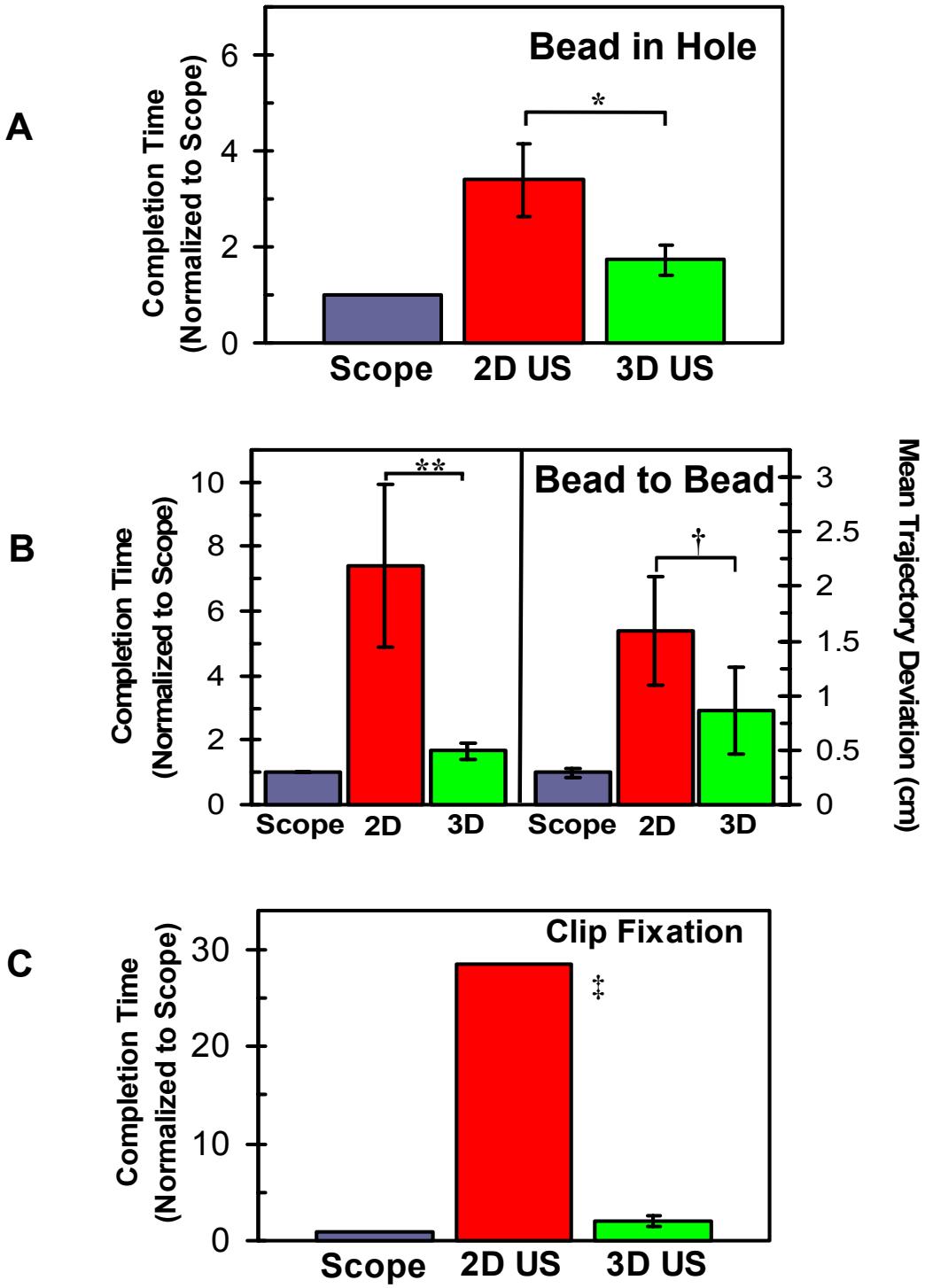

Figure 2.9 Results for 2-D vs. 3-D image-guided surgical task performance. A) Completion time for Bead in Hole Navigation normalized to endoscopic performance for 2-D vs. real time 3-D US guidance (* p=0.05). B) Completion time and mean trajectory deviation for Bead to Bead Navigation (** p=0.01; †p=0.04). C) Completion time for Clip Fixation. (‡ all subjects did not complete this task with 2-D US due to excessive completion times (≥ 270 s) and error rates.

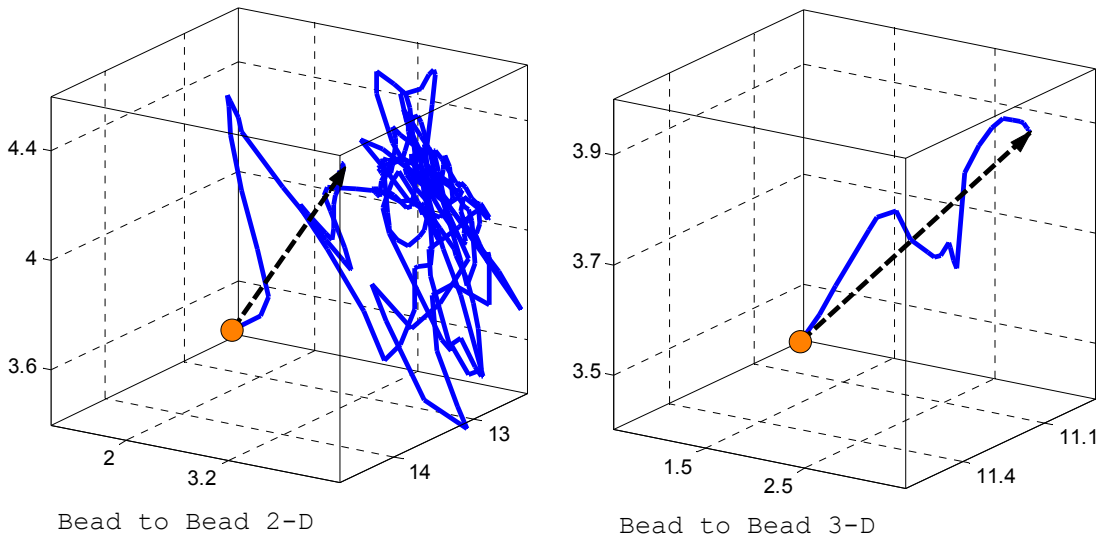

Figure 2.10 Example trajectories for Bead to Bead navigation guided by 2-D US (left) and 3-D US (right).

Table 2.1 Results for Image-guided Surgical Tasks (mean ± standard error)

Task/Imaging Modality	Completion Time (s)	D_{mean} (cm)	D_{max} (cm)
Bead in Hole			
Endoscope	2.76±0.52		
2-D	10.21±3.5		
3-D	4.19±0.63		
Bead to Bead			
Endoscope	2.05±0.32	0.30±0.04	0.92±0.18
2-D	13.29±3.69	1.62±0.35	3.55±0.78
3-D	3.19±0.62	0.87±0.22	2.12±0.74
2-D Surgeon	13.77±5.05	1.69±0.37	3.70±0.75
3-D Surgeon	4.72±1.05	0.80±0.33	1.95±0.69
Biplanar	7.10±1.33	1.25±0.77	2.70±0.82
3-D at 15°	3.80±0.91	0.91±0.27	1.99±0.46
3-D at 75°	4.62±1.28	0.69±0.15	1.51±0.28
Clip Fixation			
Endoscope	13.48±2.94		
2-D	270*		
3-D	13.48±5.82		

*Based on one task completion

Biplanar image presentation improved performance by an average of 52% over 2-D US although this improvement did not prove statistically significant (p=0.16). When compared to 3-D US guidance, however, task completion times with biplanar imaging were significantly longer (p=0.009). Tool tip deviation, on the other hand, was not significantly different when comparing either 2-D vs. Biplanar or 3-D vs. Biplanar image guidance.

Surgeon-controlled imaging did not improve task performance for 2-D US image-guided task completion (p=0.306). Similarly, there was no difference in task performance with surgeon-controlled 3-D US imaging vs. sonographer-controlled imaging (p=0.088). There was also no significant difference in D_{mean} or $D_{\max}$ for either 2-D vs. 2-D surgeon guidance or for 3-D vs. 3-D surgeon guidance.

When considering appropriate presentation of the 3-D image, changes in image perspective did not substantially decrease performance of the Bead-to-Bead Navigation task. However, during completion of this task with 3-D imaging, at times, the tool shaft or the shadow of the tool obscured the target requiring a slight shift in the US transducer or the instrument to relocate the exact position of the target. This line of sight interference occurred more frequently as the image perspective became either more horizontal (15°) or more vertical (75°) although the data did not reflect this at a statistically significant level. Trajectory analysis for each of these presentation angles showed only small differences in mean trajectory deviation again with no statistically significant difference among any of these different presentations.

Clip Fixation (Figure 2.9C) proved highly impractical using 2-D US imaging with excessive completion times (≥ 270 s) and error rates. However, when performed using real time 3-D US guidance, task completion times were similar to endoscope guidance times with very few misapplied clips (0.3±0.1 per attempt).

2.3.3 Discussion

This study examines the potential role for real time 3-D US in guiding surgical tasks with the hypothesis that additional spatial orientation information should improve performance over 2-D US guidance and may enable completion of more complex tasks using US guidance alone. Results from the validation study presented here indicate that even for basic navigational tasks, real time 3-D US can significantly improve performance over the current standard of 2-D imaging for US-guided interventions. More importantly, this study demonstrates that complex two-instrument surgical tasks (impossible with 2-D US guidance) can be performed with real time 3-D US imaging with results

comparable to optical imaging. Thus, real time 3-D US may enable minimally invasive approaches to surgical diseases in locations not readily accessible by optical imaging.

The evaluation tasks in this study represent a range of difficulty from the basic navigation tasks currently guided by 2-D US in clinical practice to a much more complex task requiring the simultaneous use of two instruments which has not previously been performed under US image guidance. Both navigation and clip fixation have direct relevance for procedures which might be performed using image-guided minimally invasive surgical techniques. Examples include fetal heart valve expansion with a catheter balloon [58], clip fixation of a repair patch to close congenital heart defects [59], or placement of a supporting ring around a dilated valve inside a beating heart [26]. For relatively simple interventional tasks (able to be performed with one instrument), this study also suggests that with 3-D US, surgeon-controlled imaging represents a safe and reliable alternative if an imaging expert is not readily available.

This study did not demonstrate any significant difference between task performance measures for images presented at different projection elevations. As the image pitch approaches either a horizontal or vertical extreme, some cues gained by a perspective view may be lost. In addition, these extreme views differ significantly from the "natural" view the surgeon would have of the operative field if observing it directly. Consequently, one would expect a unimodal histogram for all task performance measures with the best performance given by an isometric image presentation. This effect was not conclusively observed in the current study possibly due to the small number of subjects (n=7). Alternatively, surgeons may be able to infer sufficient spatial orientation data from the accessory surface shading cues present in the 3-D image regardless of the perspective angle [60].

Instrument shadowing and tools interposed between the US transducer and the target did at times limit user performance which could, in part, explain discrepancies between real time 3-D US and endoscopic performance. These limitations could be overcome by using several techniques including re-configuring the study tank so that the US transducer can be positioned opposite the surgical instruments to minimize shadowing (the image can then be arbitrarily rotated into a suitable orientation for the surgeon). Additional techniques for enhancing the surgeon's view of the operative field include image oscillation for improved perspective (periodically or a periodically rotating the image) or collocation of the US image over the operative field to simulate open surgery.

Current use of 3-D US for image-guided interventions is limited due to delays from image acquisition and processing inherent in existing systems. In contrast, the real time 3-D US system evaluated in this paper has a frame rate sufficient for working inside a dynamic surgical field, and its resolution is adequate for guiding surgical instruments. Parallel developments in image processing,

surgical instrumentation, and image presentation will also enhance performance of these image-guided procedures. With these development efforts currently underway, this imaging system has the potential to improve current interventional ultrasound techniques while also enabling new minimally invasive image-guided surgical procedures.

2.4 Conclusions

These studies performed in an *in vivo* animal model and in a surgical simulation tank clearly demonstrate the ability to perform surgical tasks including complex maneuvers with two instruments using real time 3-D US for image guidance. As shown in both of these studies, 2-D US proves inadequate for guiding the required tasks for performing surgery inside the heart. The animal model demonstrated the indispensable need for understanding spatial relationships inside the heart in order to perform procedures safely and accurately while the tank study quantified this requirement.

In addition, both studies revealed many aspects of the current 3-D US system and of this initial surgical approach which require further development and improvement. First, as with any surgical procedure, especially inside the heart, patient safety remains the most important factor. In the current setup, the surgeon is fully dependent on the rendered US image to perform the surgical task. Unlike laparoscopic surgery with a videoscopic image where many accessory visualization cues are available to the surgeon, the surgeon has limited accessory cues in these cases. Thus, all information regarding tool location, location of the target tissues, and the location of other nearby important structures must be inferred from the volumetric US image. In cases of significant acoustic shadowing and other forms of data loss or artifacts, the safety of the procedure is compromised.

Another significant limitation of this approach relates to large-scale instrument movements. When the surgeon first introduces a surgical instrument into the heart chamber, the tool tip is no longer visible; so the surgeon must try to "blindly" find either the internal target or the region inside the heart currently being imaged. Ideally, the sonographer would be able to direct the US probe towards the entry site and follow the instrument into the heart so that it remains in view at all times. However, this scenario rarely proved possible in the animal procedures due to limited "standoff" between the insertion site and regions on the heart available for direct epicardial imaging. In addition, because the US image can be rotated in any arbitrary direction, the view is not always intuitive for the surgeon. These factors combine to add significant delays to the procedure and increased frustration for the surgeon. Similar challenges were noted by four of seven subjects in the tank study despite the fact that in each procedure, the tool started well within imaging frustum (if the instrument went outside the field of view, it proved difficult to then re-gain orientation).

To address these issues of procedure safety and surgeon orientation, the following two chapters discuss techniques for enhancing the view of the operating field seen by the surgeon on the US display. Two primary techniques have been applied to these volumetric US images for this purpose: image segmentation (Chapter 3) and atlas-based model-matching (Chapter 4). In these chapters, the application of these techniques to US imaging is illustrated in detail with examples and practical demonstrations related specifically to these two issues.

3 Segmentation Techniques for Real-Time Volumetric Ultrasound Imaging

IMAGE segmentation represents a number of diverse tools for deriving information from image data. As with many current image-guided procedures, image segmentation will likely play a fundamental role in beating heart intracardiac procedures as well. The imaging modality we are currently using for these procedures presents several unique challenges due to the specular nature of US imaging, the fact that the surgical target is constantly in motion, and because of the high volume of data that must be processed to keep pace with the procedure. In this chapter, a brief overview of medical image segmentation is presented followed by a discussion of manual segmentation and its potential role in these procedures. Subsequently, the challenge of the extremely high bandwidth of real time 3-D US is addressed by with the application of an computationally efficient active contour model for image segmentation. Performance of this model is then quantified using phantom models as well as US images of the heart. In the final section, application of this segmentation approach to US-guided heart surgery is addressed.

3.1 Medical Image Segmentation

Image segmentation is the process of grouping image data into meaningful regions [61]. This generally involves a partitioning process where the original image points are divided into subsets corresponding to anatomic structures. In the heart, this might involve identifying the valve leaflets or support structures as separate from the heart wall or the blood pool inside one or more of the chambers. This process can be divided into three major categories depending on the level of user input: 1) manual segmentation, where the user identifies structures within the image; 2) semi-automatic segmentation, where the user initiates a process which then proceeds to identify the relevant

region; and 3) automatic segmentation, where some process identifies relevant regions with minimal user interaction or input.

Because of the complexity of medical images and the diversity of structures, segmentation is generally performed either manually or using some type of semi-automatic technique. For volumetric images, performing manual segmentation by identifying region boundaries either on every planar image slice or on several representative slices is extremely labor intensive and time-consuming. Furthermore, manual slice segmentation suffers from the drawbacks of inter-user variability as well as operator bias and fatigue. Nonetheless, some argue that for US imaging, this approach is the only reliable method [62].

For imaging modalities with high contrast among tissue types such as CT or MRI, intensity-based methods which use statistical classification work reasonably well. Examples of classifiers include simple thresholding, maximum likelihood (ML) classifiers, those based on *a posteriori* probability called MAP classifiers, and *k*-nearest neighbor (kNN) classifiers. For US images, these methods could be used to segment the blood pool from the heart structures provided artifacts and dropout of physical structures are minimal.

For US images, deformable model segmentation approaches can overcome many of the limitations of manual slice editing and the more traditional image segmentation techniques described above. These continuous geometric models can compensate for noise, gaps and other irregularities in region boundaries. Furthermore, both the parametric and level-set (geometric) mathematical representation of the models afford a compact, elegant description of object shape. These properties lead to a robust method for connecting sparse or noisy local image features into a coherent and consistent model of the object region [63].

3.2 Manual Segmentation of Volumetric US Images

Manual segmentation is still used widely in medical image analysis for quantitative diagnosis and surgical planning. In addition, it is unlikely that semi-automatic segmentation or automatic segmentation schemes will work in every situation where volumetric US image segmentation is required for guiding intracardiac procedures. Thus, this section describes a simple software tool that was developed for manually segmenting volumetric US images. A brief summary of the uses for this tool throughout this thesis is then provided at the end of this section.

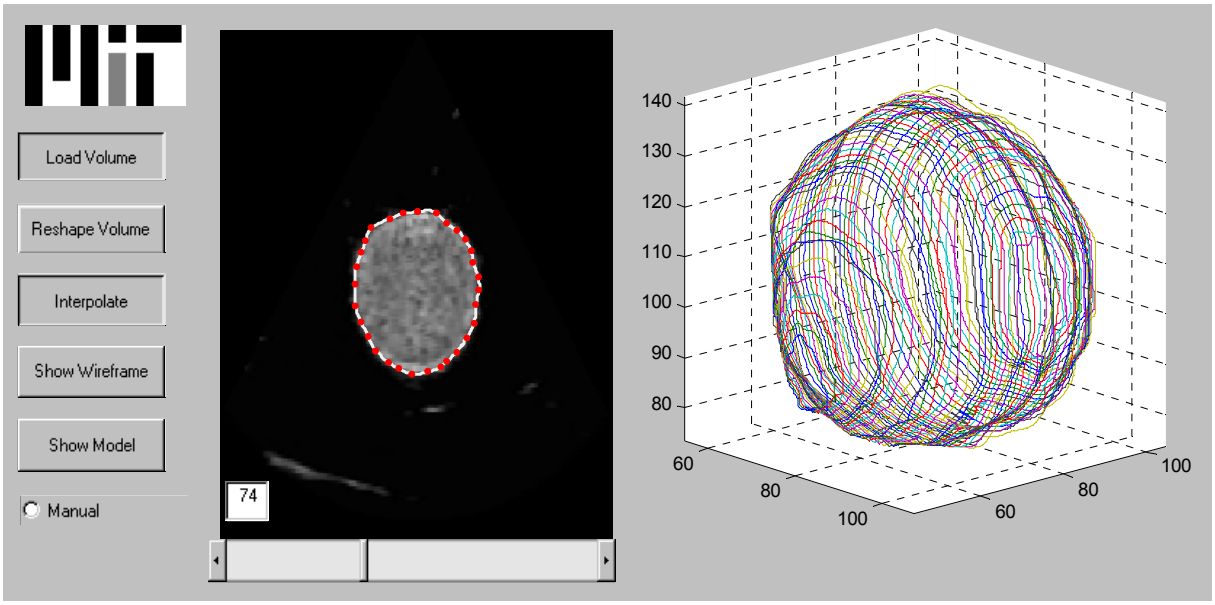

Figure 3.1 Manual Segmentation User Interface. In this example. an US image of a spherical tissue phantom has been loaded and 30 control points were selected along the phantom border at 10 representative slices (out of 60). The remaining slices were interpolated and a wireframe model of the phantom is displayed to the right.

3.2.1 User Interface and Tool Functionality

This interface and the others presented in this thesis were developed in MATLAB (version 6.5.0) and were run on laptop computer with a 1 GHz Pentium III processor. As depicted in Figure 3.1, the user interface for manual segmentation includes basic controls for loading the volume, reshaping the volume, acquiring data points specified by the user, and then displaying either a wireframe model or a rendered polygonal mesh model of the segmented object.

In contrast to previous 3-D US images acquired by aligning multiple 2-D slices, the data set from this imaging probe is acquired by a 2-D phased array. As previously shown, the volumetric data set ranges in size from 128x48x208 to 160x144x208. In both cases, the axial-direction is super-sampled so that the largest dimension (208 in these cases) lies along the axis of the probe. Thus, the most intuitive means of presenting the slice-by-slice images from this volumetric data set is as if the probe is positioned at the top of the image with one of the lateral dimensions forming the other axis of the image. This is depicted in Figure 3.2. Then, using a scrollbar, the user can pan through the volume slice by slice moving forward or backwards along the other lateral direction. In this interface, the user can select an US image volume to load and then can either display the volume in its default orientation or can use the “Reshape Volume” button to permute the principal axes and thus reset the view.

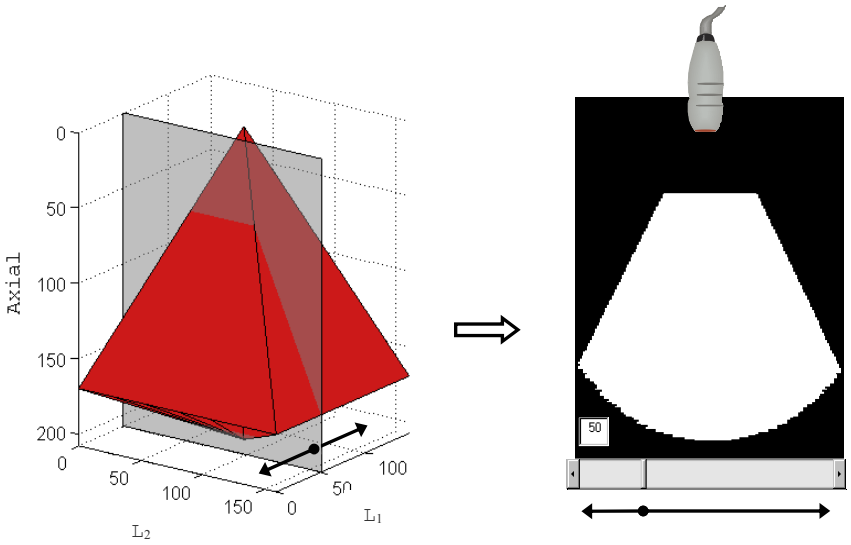

Figure 3.2 Nomenclature and orientation for image presentation in the user interface.

The data point selection is achieved by calling the `ginput` function in MATLAB which then allows the user to select points along the boundary of interest. The selected point is then plotted on the same image slice (red 'o' in Figure 3.1). When the user completes the selection process, the coordinates of each control point are used to interpolate a cubic spline with ten times the resolution of the original control points plotted as a smooth curve through the original data points.

In this fashion, the user can step through the entire volumetric data set and perform the same process at every slice or on a representative sub-sample of slices. In the latter case, the "Interpolate" control is activated to linearly interpolate a wireframe at each intermediary slice. Correspondence is governed by control point order. Because most of the images and structures described in this work have a simple topology, there was no need to infer the intermediary wireframe using other techniques such as distance transforms [64] or maximal disk-guided interpolation [62].

3.2.2 Applications for Manual Segmentation

Scaling Factor Determination and Control Point Selection

Volume measurement is an important quantitative tool for any 3-D US system which also serves as an indirect measure of the accuracy of the physical boundary detection of other segmentation approaches. To relate pixel dimensions to physical dimensions for this purpose, the image scaling factor must be determined. A method for easily and repeatably performing this measure in 2-D US has been described [65] which was directly extrapolated to 3-D for this purpose. This technique assumes isotropic scaling in the post-scan converted data which can be related to physical units by imaging a

feducial marker board. The board contains three markers at known (and preferably distinct) distances from one another. Multiple images of this board containing all three markers are obtained. These images are then loaded into the manual segmentation tool, and the center of each marker is selected. The Euclidian voxel distance between the markers is then calculated and converted to distance dimensions using the known separation between each marker. For the studies presented in this thesis (EKG-gated "full volume" images), the scaling factor was found to be 0.079 ± 0.002 cm/pixel based on three independent measurements.

Similarly, this manual segmentation tool can be used to select anatomic structures within the volumetric data set. By scrolling forward and backward through the volume, the user can identify important landmarks which can then be assembled into an array of homogeneous vectors. These landmarks can then be used as control points for registering a graphical model to the patients heart structure as detailed in Chapter 4.

Volume Measurement Comparison and Validation

Manual segmentation also serves as a baseline performance measure for other segmentation techniques. Despite the drawbacks of this technique outlined above, it remains the gold standard method for medical image segmentation against which others are compared. In this thesis, volume measurements of spherical phantoms are performed using both manual and semi-automatic segmentation (Section 3.4) as an indication of the quality of the semi-automatic segmentation method described below. Subsequently, manual segmentation serves as the performance standard for this semi-automatic segmentation method applied to a heart chamber where the physical volume is not known.

3.3 Active Contour Segmentation of Volumetric US Images

Active contour models, commonly termed snakes, have proven useful for a range of medical image analysis applications [63, 66]. As originally described by Kass, Witkin and Terzopoulos [67], this semi-automated approach to image segmentation employs a Lagrangian formulation from classical mechanics to identify relevant image features based on intrinsic image "forces." This approach is useful for segmenting noisy images where no a priori knowledge of the object of interest is required.

The original formulation of this methodology and subsequent variations on this approach include minimization terms which work at odds against one another leading to long computation times. Other semi-automatic segmentation methods including model-based segmentation [68], level sets [69-71], and deformable surfaces [63, 72] have also been extensively applied to medical imaging. While these

methods lead to anatomically accurate results, the computation times required range from minutes to even hours.

In a separate body of work, Perrin has implemented a new snakes algorithm which retains the attractive features of active contour models with greatly improved computational efficiency [52, 53]. Initial assessment of this approach by the author indicated sufficiently fast segmentation times to be applied to real time volumetric imaging. In this section, the traditional snakes formulation is briefly presented along with this new snakes formulation. A description of the author's use of this new algorithm for segmentation of volumetric US data is then presented in detail.

3.3.1 Methods

Segmentation of streaming volumetric image data represents an important step to enabling rapid diagnosis and accurate medical interventions. To reduce the computational expense of traditional active contour models for these types of applications, a more efficient segmentation algorithm was recently developed by returning to the original motivations behind classical snakes.

Re-formulated Classical Active Contours for Fast Segmentation

An active contour model is a parametric curve

$$S(u) = I(x(u), y(u)) \tag{3.1}$$

in the image plane $(x, y) \in \mathbb{R}$ on the interval from 0 to 1. This curve is allowed to deform within the potential field derived from the image in an attempt to minimize its energy, where

$$E = \int_0^1 [E_{int}(S(u)) + E_{img}(S(u))]du \tag{3.2}$$

In the original formulation, E_{int} consisted of a weighted sum of a tension term to evenly space control points along the curve and a stiffness term designed to maintain local smoothness by minimizing curvature

$$E_{int} = \alpha \oint \left\| \frac{\partial}{\partial u} S(u) \right\|^2 du + \beta \oint \left\| \frac{\partial^2}{\partial u^2} S(u) \right\|^2 du \tag{3.3}$$

where α is the tension weighting factor, β is the stiffness weighting factor and $\|\bullet\|$ is the Euclidian norm. The other term in (3.2), E_{img} is the potential induced by the image values originally defined as the result of edge detection.

This formulation contains several problematic features. First, the tension term is included to allow the snake to "explore" the image space; however, the approach outlined above acts to push the contour towards a minimum length thereby collapsing the curve as it seeks to evenly space the control points. Second, the stiffness term was intended to produce a locally smooth contour. By minimizing curvature, this goal is achieved, but this approach forces *all* contours towards a straight line.

To achieve a locally smooth result with evenly distributed control points, Perrin first re-examined the classical approach which defines "smooth curvature" as a zero second derivative. The force resulting from this term will go to zero only when the curve forms a straight line. Alternatively, consider the case of a *constant* third derivative. If the force is allowed to go to zero in this case, smoothly changing curves such as a spiral of constantly increasing or decreasing radius or a circle would produce little or no energy. Thus, rather than minimizing curvature, we minimize

$$E_{smoothing} = \beta \oint \left\| \frac{\partial^3}{\partial u^3} S(u) \right\|^2 du \,. \tag{3.4}$$

To prevent the snake from collapsing inappropriately, the *pressure snakes* method of Ivins and Porrill [73] (based on the early work of Ronfard [74]) was adopted. In this approach, a seed region is selected within the target with *no* requirement that this region approximate the target's boundary. From this seed region, the mean (μ) and standard deviation (σ) of the image intensity values then contribute to an inflationary/deflationary energy term $E_{pressure}$ given by:

$$E_{pressure} = \rho \left(\frac{\partial}{\partial u} S(u) \times S(u) \right) \left(1 - \frac{|I(S) - \mu|}{k\sigma} \right) \tag{3.5}$$

where ρ is a constant and k represents the number of standard deviations away from the mean intensity of the seed region which produces an inflationary/deflationary force.

The implementation of these two terms is computationally efficient with details presented in [53]. Curve smoothness is measured using five control points centered on the control point currently being updated. By examining the exterior angles θ_i formed by the three line segments between these control points, a constant third derivative is produced when the middle control point is moved to a new location such that (3.6) is satisfied:

$$\theta_2' = \frac{1}{3} \sum_{i=1}^{3} \theta_i \tag{3.6}$$

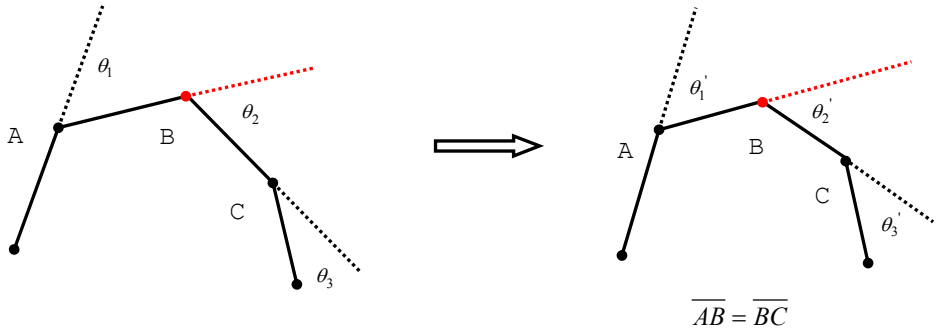

Figure 3.3 Strategy for adjusting control points along the curve which leads to a locally smooth contour with evenly spaced points.

where $\theta_2^{'}$ is the value of the updated external angle at the middle control point (Figure 3.3). In addition, using this approach to guide control point adjustment (with the perpendicular bisector of $\overline{AC}$ as the iterative target for *B* in this example) leads to even spacing which was one of the original goals of the classic tension term. Thus, this iterative smoothing approach produces a locally smooth curve with evenly distributed control points. The complete model is then achieved by adding the $E_{pressure}$ term above.

Applications to Ultrasound Data

In this study, we sought to determine both the accuracy and the speed of this new segmentation algorithm. Accuracy was determined by comparing volume estimates based on image segmentation to known volumes of US phantoms. Furthermore, the speed of this iterative segmentation algorithm was tested on both US phantoms and on volumetric cardiac US data to determine the potential for applying this approach to image-guided cardiac surgery. For these evaluations, another user interface was designed to facilitate ready adjustment of the contour parameters, *k*, β, and ρ; to track iteration numbers, and to compute object volumes.

Using the scaling factor derived above, volume estimation was used to test the accuracy of this segmentation algorithm. Six balloon-shaped phantoms made from tissue-mimicking gelatin [75] were imaged in a degassed water bath as described in Chapter 2. These images were then segmented both manually and with the revised active contour model. In the latter case, segmentation was performed by seeding the contour within a slice in the middle of the volume and then propagating the incremental

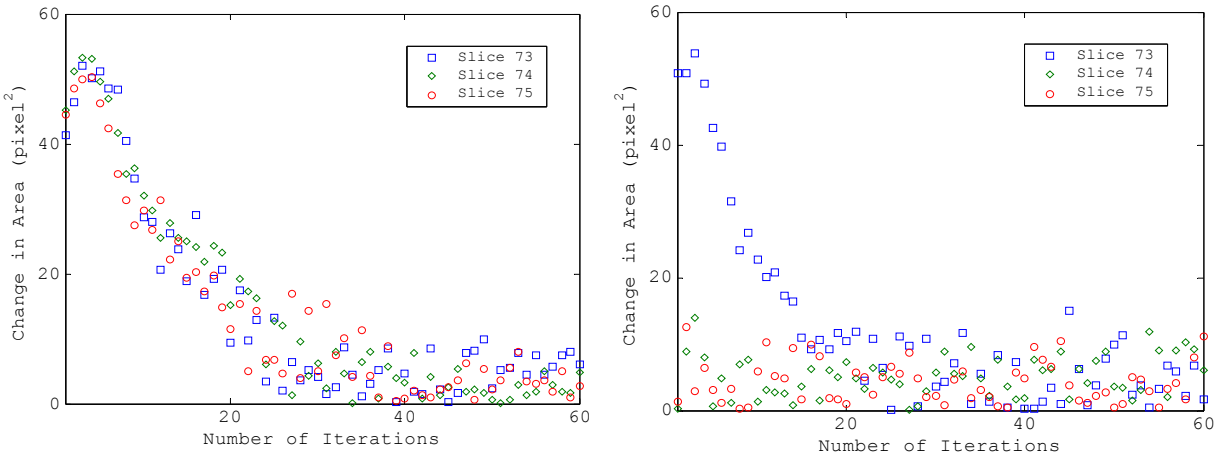

Figure 3.4 Convergence of the active contour in three adjacent slices using independent contours to seed each slice (left) vs. seeding each adjacent slice with the contour from the previous slice (right). In the latter case, the contour is seeded in `Slice 73` with then converges. This converged contour then seeds `Slice 74` and so on iteratively.

converged contour both forwards and backwards through the volume. As shown in Figure 3.4, there is an important time savings in using the converged contour for each slice to seed the next adjacent slice. The phantom volume is then obtained by summing the area enclosed by each curve multiplied by the uniform "thickness" of each slice.

To further test the accuracy of this segmentation approach, 3-D US images were taken of a porcine heart from a 40 kg animal. This heart filled with pressurized saline inside a water bath, and the images were acquired from an anterior perspective so that the entire left ventricle was fully contained within the data set. The segmentation algorithm was then applied to the gridded Cartesian data (160x144x208) using the same approach as described above. For this test, tight convergence measures for the curve were employed to ensure accurate localization of the heart wall. These included both a control point distribution measure and a measure of the change in area inside the curve. Timing tests were performed on an Athlon 1.2 GHz PC running Mandrake Linux 9.0.

3.4 Manual vs. Semi-Automatic Segmentation

The results for segmentation of six balloon-shaped phantoms ranging in volume from 38-56 ml is shown in Table 3.1. The actual volume vs. volume estimation by segmentation showed a high degree of correlation as illustrated in Figure 3.5. However, there was more variability in the results from manual segmentation leading to a smaller r^2 value than for the snakes segmentation approach.. Volume calculations based on manual segmentation ranged from -5.8% to 15.8% compared to the measured volume of each phantom (95% confidence interval -3.3% to 8.0%). For the snakes segmentation,

Table 3.1 Comparison of Volume Measurements by Manual vs. Snakes Segmentation

PHANTOM	VOL. BY WEIGHT (CC)	VOL. BY MANUAL SEGMENTATION (CC)	% DIFFERENCE (MAN. VS. WT.)	VOL. BY SNAKES SEGMENTATION (CC)	% DIFFERENCE (SNAKES VS. WT.)
1	49.45	49.40	-0.1%	48.94	-1.0%
2	54.55	51.37	-5.8%	55.57	1.9%
3	37.36	37.82	1.2%	38.01	1.7%
4	42.27	41.04	-2.9%	42.34	0.2%
5	37.73	43.69	15.8%	38.22	1.3%
6	46.90	49.73	6.0%	46.25	-1.4%
95% CI			**-3.3% to 8.0%**		**-0.6% to 1.5%**

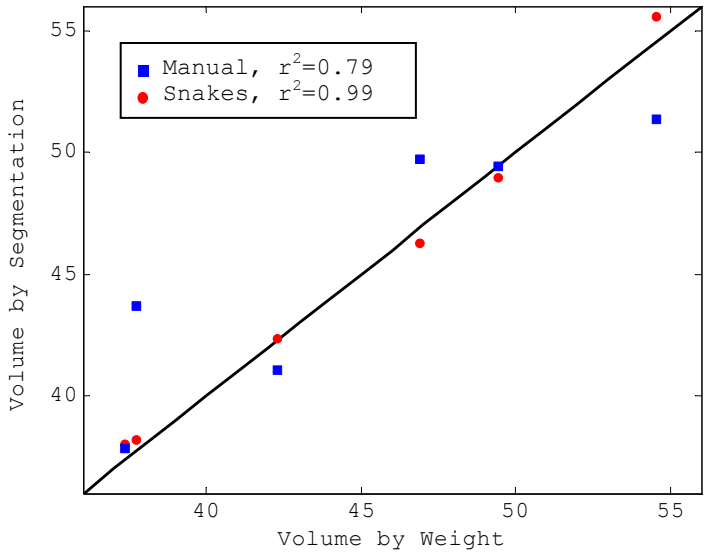

Figure 3.5 Correlation of segmentation volume to known volume of the phantom as measured by weight. Semi-automatic segmentation showed a stronger correlation than manual segmentation.

Table 3.2 Time Required to Perform Segmentation

PHANTOM	MANUAL	MANUAL + INTERPOLATION	SNAKES
1	1684 sec	203 sec	40.2×10^{-3} sec
2	-	185	46.2×10^{-3}
3	-	196	42.3×10^{-3}
4	-	199	35.6×10^{-3}
5	-	158	35.6×10^{-3}
6	-	189	41.2×10^{-3}
Mean ± SEM	-	**188±7**	**$40.2 \pm 1.7 \times 10^{-3}$**

volume estimates ranged from only 1.4% less than the known volume of the phantom to 1.9% over the known volume of the phantom (95% confidence interval -0.5% to 1.5%).

Obviously, manual segmentation requires much longer than the semi-automatic snakes approach with the results explicitly summarized in Table 3.2. While complete manual segmentation required in excess of 28 minutes, using interpolated wireframes reduced this time to just over 3 minutes on average. Meanwhile, the snakes segmentation approach performed this process on the order of 40 milliseconds which is fast enough to segment twenty-five such US volumes each second. The results of manual segmentation with interpolation and snakes segmentation of the US phantoms are presented as rendered surfaces in Figure 3.6.

Similar comparisons were performed on images taken of a fresh pig heart as described above. Manual segmentation was performed on ten evenly spaced representative slices from the image volume with the intermediary wireframes obtained by interpolation. For the snakes segmentation a single short-axis slice through the mid-portion of the left ventricle was used to determine the image

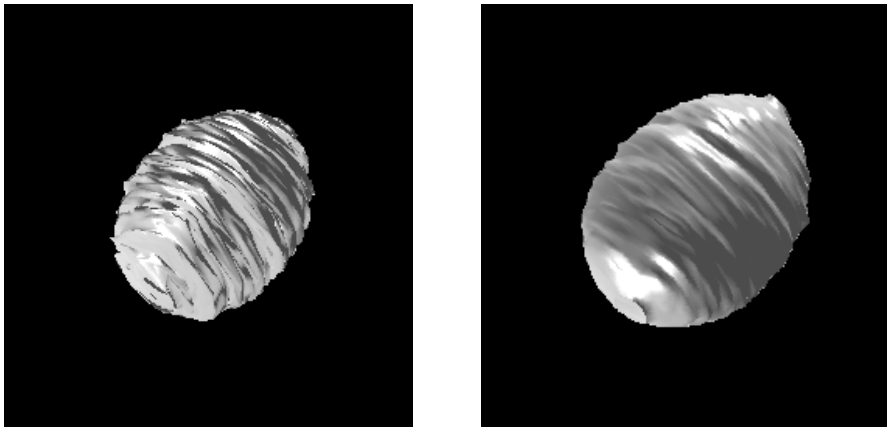

Figure 3.6 Rendered surface model of a balloon-shaped phantom segmented manually (left) vs. using the snakes algorithm described above (right).

statistics and to seed the snake (Figure 3.7A). Subsequently, the contour identified the endocardial border (Figure 3.7B) after 50 iterations requiring a total of 0.0045 seconds. This contour was then used to seed the adjacent short-axis slices and allowed to converge. These incrementally converged contours seeded each adjacent slice until the entire ventricle had been segmented. The final segmented volume spanned 80 image slices and measured 30.84 cc (compared to 30.94 cc measured by manual segmentation with interpolation). This entire segmentation process required a total of 0.0425 seconds while the manual segmentation process required over three minutes. The results of both segmentations appear in Figure 3.8.

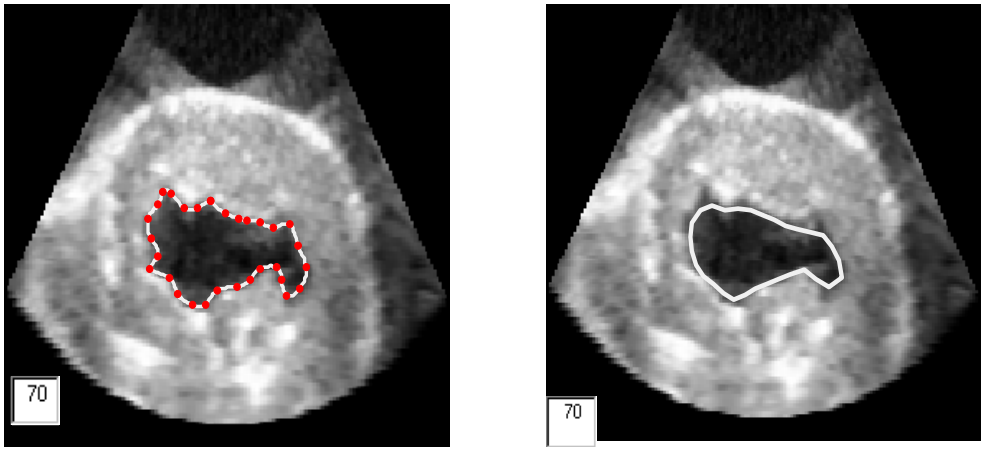

Figure 3.7 Comparison of manual (left) vs. snakes (right) segmentation. Both images are of the same slice in the image volume of left ventricular cavity of a pig heart, and both contours use thirty control points.

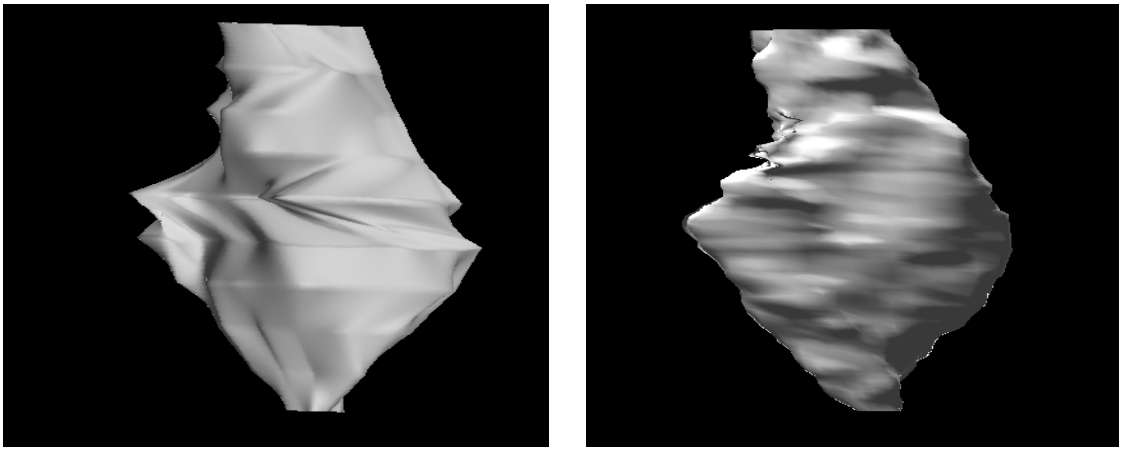

Figure 3.8 Segmented ventricular cavity comparing manual segmentation (left) to snakes segmentation (right). The manual model required over three minutes to obtain with the longitudinal striping effect caused by slight mismatches in control point correspondence. In contrast, the snakes segmentation algorithm required only 42.8 ms.

3.4.1 Discussion

By re-formulating the original implementation of the active contour model, Perrin achieved significant improvements in computation time opening a number of applications for real time processing of both planar and volumetric image data. This algorithm proves both highly accurate with the ability to segment an entire phantom and the endocardial surface of the heart in a fraction of a second. This represents about an order of magnitude improvement in speed over any previous results. Furthermore, this result is obtained with minimal user input consisting of the user indicating the seed region at some place in the middle of the object of interest.

Compared to other recent reports of volumetric medical image data segmentation, this approach represents a significant time savings. These other approaches include model-based segmentation methods [68, 76], level sets [70], and deformable surfaces [72]. Although these approaches lend themselves well to segmenting dynamic objects in three spatial dimensions, the computational expense remains too high for real time volumetric applications.

This study contains several limitations. First, the volume estimation is based on gelatin phantoms in an imaging tank. In addition, the image data sets used for this study are similar in size to pediatric heart data sets which is the primary focus of this group of investigators. Much of an adult ventricle can be captured with the current imaging system using beam steering, but this data set is not currently available as a real time imaging mode.

Future investigations stemming from this work include further integration of the segmentation process with the imaging system. This will proceed as we begin to apply this approach to in vivo clinical images as the imaging system undergoes further evolution. These future changes include optimization of the acoustic transmit power and gain settings to limit problems of data dropout. In addition, integrating the segmentation software with the image gating will allow online cardiac ejection fraction estimation.

This segmentation approach has applications for real time medical image analysis which extend far beyond diagnostic quantitative echocardiography. Examples include uses in the operating room when the heart is weaning from cardiopulmonary bypass to determine real time ejection fraction, development of virtual fixtures for robot-assisted image-guided interventions, and real time instrument tracking during surgical procedures.

3.4.2 Conclusions

The use of a computationally efficient active contour model can be applied to medical image analysis for real time volumetric segmentation. The results presented here illustrate both the accuracy and tremendous speed of this algorithm. Although the results presented here relate most directly to quantitative echocardiography, the implications of this approach extend both to other imaging modalities and to other applications such as image-guided interventions.

3.5 Application to Image-guided Intracardiac Surgery

One application of this technology involves using the imaging data to set boundaries beyond which the surgeon receives a warning or robotically-controlled instruments cannot navigate, a process of creating "virtual fixtures" [77]. In addition to clearly demarcating danger regions within the surgical field, these fixtures allow the surgeon to work more efficiently by using the fixture as a guide, much as a ruler is used to improve the speed and accuracy in drawing a straight line. This approach has been used in orthopedic procedures [78] and for mammary artery harvesting (the first step in CABG procedures) [79]. Similar augmented reality surgical techniques have also been described for neurosurgery [80] and breast surgery [81]. However, the application described here goes beyond this previous work in that the graphical image is updated at 20-25 volumes per second in order to maintain an accurate boundary throughout the surgical procedure.

For this demonstration, a volumetric US image of the Left Atrium of a healthy volunteer was obtained using conventional trans-thoracic imaging techniques with a representative slice shown in Figure 3.9. The snakes segmentation technique described above is then applied to this region with the

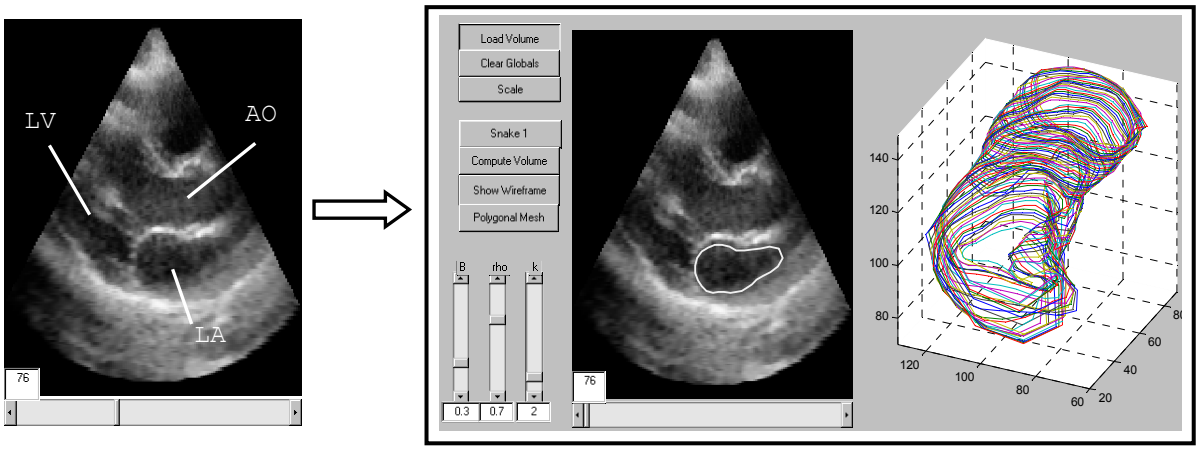

Figure 3.9 Planar US image of the left atrium (LA) and left ventricle (LV) taken from a volumetric image. This image volume was then segmented to reveal the atrial wall.

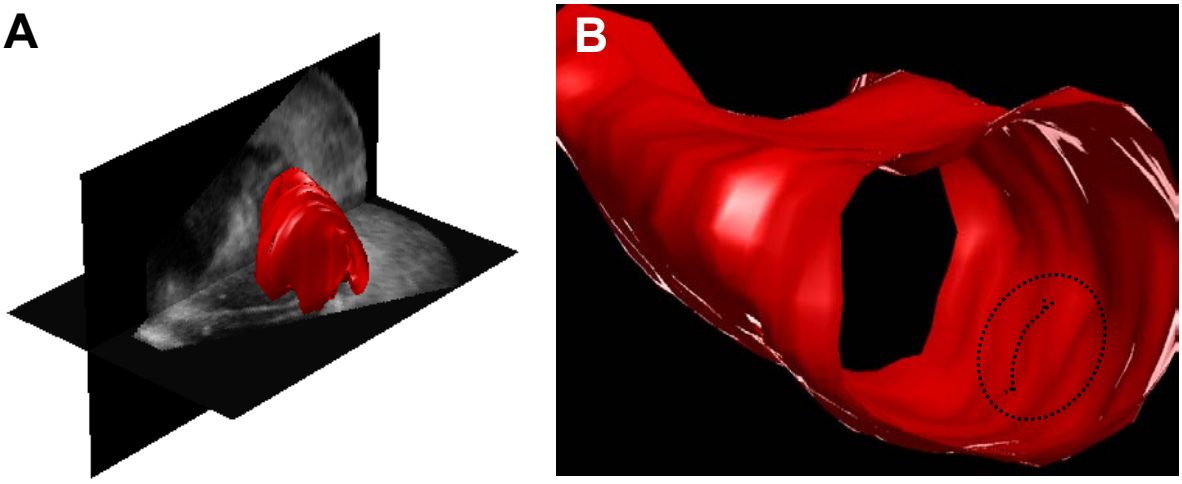

Figure 3.10 A) Segmented atrial chamber displayed within the US volume. B) Cut-away view of the segmented atrial chamber in which surgical instruments can be animated.

iteratively converged contour used to seed adjacent slices. Using the same point spread and area change convergence measures as used above, the total number of iterations to achieve this segmentation was 517 which can be performed in 46.4 ms. The rendered model of the atrial chamber is displayed in Figure 3.10A with a cut-away of the graphical model shown in Figure 3.10B. By calibrating the US system at the beginning of the surgical procedure and then referencing both the images and tracked surgical instruments to a common coordinate frame, the instruments can also be displayed within this model. Intraoperatively, the US image and this graphical model fixture can be displayed either together in a single display or side-by-side in separate frames. In addition, the model can be rotated in any arbitrary direction giving the surgeon the needed reference points for determining depth of field within the 3-D model.

4 Atlas-based Model Matching as a Navigational Aid

BECAUSE of the limited size of the image frustum, accurately navigating instruments into the real time 3-D US field of view proved a significant challenge in the early pilot procedures. In contrast, when 3-D US was combined with a graphical model of the tool location and the target site, navigating the tools into the US field of view was straightforward. Although this augmented view of the heart chamber was presented on separate viewing monitors using completely separate software and hardware to perform the surgical task, using these displays together made the procedure more efficient and intuitive for the surgeon. Others have also found graphical navigational aids useful during surgical procedures including US/MRI-guided neurosurgery [82] and a navigational tool for orienting US images obtained from a laparoscopic probe [83]. Together, these reports along with our own findings motivated an integrated display of the heart chambers with the US image. This chapter discusses the two-step process used to achieve this goal: 1) develop a single complete volumetric image of the patient's entire heart using by spatially compounding several US data sets and 2) identify anatomic landmarks within this composite volume using manual segmentation to then register an atlas-based model of a human heart to this data set. The approach outlined in this process is specifically designed for use in an operating room setting on a patient with no other pre-operative imaging studies such as an MRI. Thus, this approach relies solely on US imaging and uses the fastest, most stable algorithms whenever possible.

4.1 Motivation

As initially described in Chapter 2, both the *in vivo* animal experiment and the tank study revealed an important limitation with using 3-D US for guiding surgical procedures. Any time the surgical instruments are outside the imaging field, it is quite difficult to re-position them within the imaging

field so that the procedure can proceed. In laparoscopic procedures, when the surgeon loses orientation and has difficulty re-positioning one or both instruments in the field of view, the camera operator simply zooms out and pans the camera until the instrument is located. The surgeon then moves the instrument together with the camera back to the working area. During US-guided heart surgery, such maneuvers simply are not possible due to limited space within the heart chamber, the need to maintain contact with the heart surface to obtain an image, and the inability to "zoom out."

Providing the surgeon with a redundant display of the operating field eliminates this problem so long at the alternative display accurately depicts the relationships between the instruments and the surgical site. To test this hypothesis that this auxiliary display would facilitate navigation during US-guided procedures, we performed a series of three beating heart surgical procedures with US guidance combined with the CARTO electromagnetic mapping and navigation system [55-57]. As described previously, this catheter-based system both maps the heart surface to create a graphical model within which the tracked catheter is then animated. The surgical setup for these procedures is shown in Figure 4.1 with the US system in the foreground and the CARTO display seen in the background. A typical map of the right atrium is also presented in this same figure.

As shown in the previous results, using this graphical model facilitated ASD creation in these three procedures. Qualitatively, each ASD was centered within the septum, and problems of identifying the tool within the US field were minimized. Functionally, the US system was used more to confirm contact with the atrial septum and less as the primary navigational means. This section

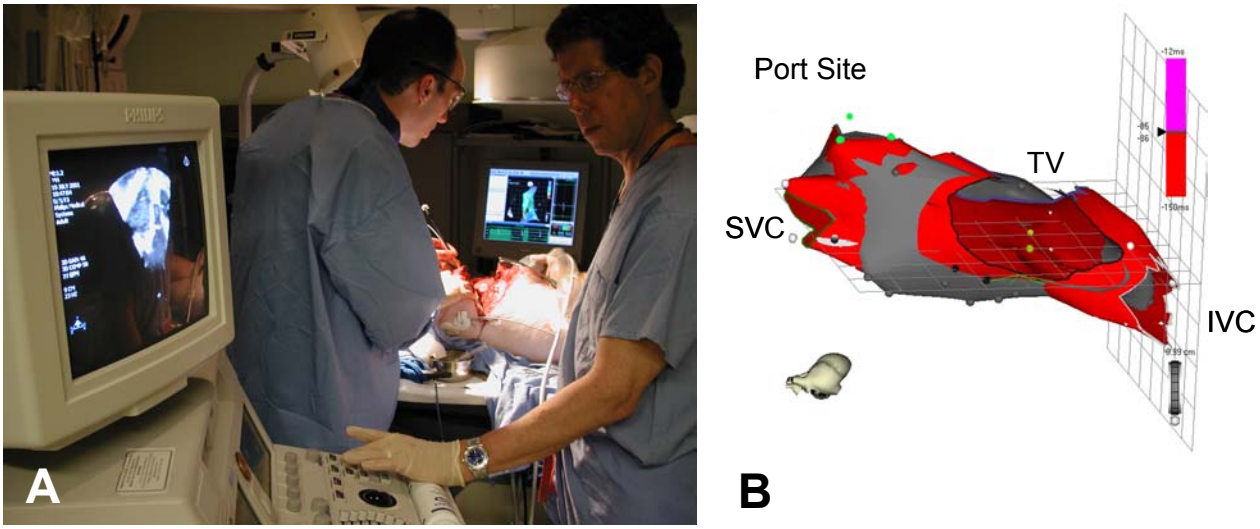

Figure 4.1 A) Surgical setup using the CARTO system as an accessory display for instrument navigation. The US display is seen in the foreground with the CARTO system positioned across the room in the background. B) Typical registered model of the right atrium produced using the CARTO catheter. The yellow markers below TV indicate the target for making an ASD. SVC=superior vena cava; IVC=inferior vena cava; TV=tricuspid valve.

describes the initial attempt to integrate this type of augmented navigational aid into the US imaging system.

4.2 Spatial Compounding

The goal of this approach is to register a graphical model of a human heart to patient-specific US landmarks so that the major anatomic features of the model are scaled and oriented appropriately for surgical guidance. Within the heart, usable landmarks for registration include the apex, the papillary muscles, the valve structures, and the inlets of the major venous structures. These landmarks are separated by as much as 15 cm which is the upper limit of the axial range for this current imaging probe. Thus, to capture all of the required landmarks within a single image volume, multiple views of the heart were taken and then combined to form a composite view.

Multiple sources of "variation" between volumetric US images of the same object making US-US registration especially difficult [84]. These sources of variation include directional variations which cannot be compensated for by applying the appropriate rigid transformation (due to shadowing, for example); "volumetric variations" due to depth gain compensation (DGC) and gain distortions; and variations due to organ movement between acquisitions. Notwithstanding, Aiger, et al chose an intensity-based approach to register multiple US volumes [84]. Other techniques have also been described including point-based registration [85], landmark detection [86], and mutual information [87]. For this work, we chose to use a six degrees of freedom (DOF) electromagnetic (EM) tracking device for combining these multiple images into a composite view understanding the potential limitations of relying on tracker data alone. The specific methods and results of this approach are given below.

4.2.1 US Probe Tracking

For this study, the miniBird 800 (Ascension Technology Corp, Burlington, VT) EM tracking device was fixed to the US transducer. Performance parameters of this equipment include full six DOF sensing with RMS static positional accuracy of 1.8 mm and resolution of 0.5 mm. Angular RMS accuracy is 0.5° with a resolution of 0.1°. The 8 mm x 8 mm x 18 mm sensor is fixed to the US probe using thermal sensitive splinting material (Aquaplast, Sammons Preston Rolyan, Bolingbrook, IL) as shown in Figure 4.2.

The tracking equipment outputs the homogeneous transform matrix ${}^{T}T_{S}$ between the electromagnetic transmitter, T and the sensor, S attached to the US probe. This data can be acquired as

either individual data points or as a data stream. In this study, the tracking data was acquired synchronously with each US image acquisition.

4.2.2 Mosaic Volume Creation

To create the composite volume, a four volumetric US images gated to the EKG were acquired of the left ventricle, right ventricle, left atrium, and right atrium in series. Then, using the MATLAB functions `maketform`, `makeresampler`, and `tformarray` each of these volumes was transformed into a common coordinate frame by applying the 3-D homogeneous transform matrix ${}^{T}T_{S}$ corresponding to each of the four volumes. In this process, each volume is transformed and the new intensity values are computed using trilinear interpolation and padded with zeros to form a new image measuring 200x100x200 voxels. In total, this process takes just over six minutes on a 1 GHz Pentium III laptop PC.

A new 4-D array consisting of these four transformed volumes is then formed and from this a composite image is generated using one of two strategies. In [86], Rohling suggests that a weighted average approach to US image compounding results in reduced speckle and reveals tissue structures more readily. Thus this approach was implemented and compared to the more basic approach of taking the maximum intensity value among the four volumes at every voxel. In comparing these two algorithms, the first took over ten minutes to raster through each voxel and perform the weighted average. In contrast, the maximum intensity method required less then twenty seconds. Furthermore, the weighted average method showed the seams between active image areas in the various volumes

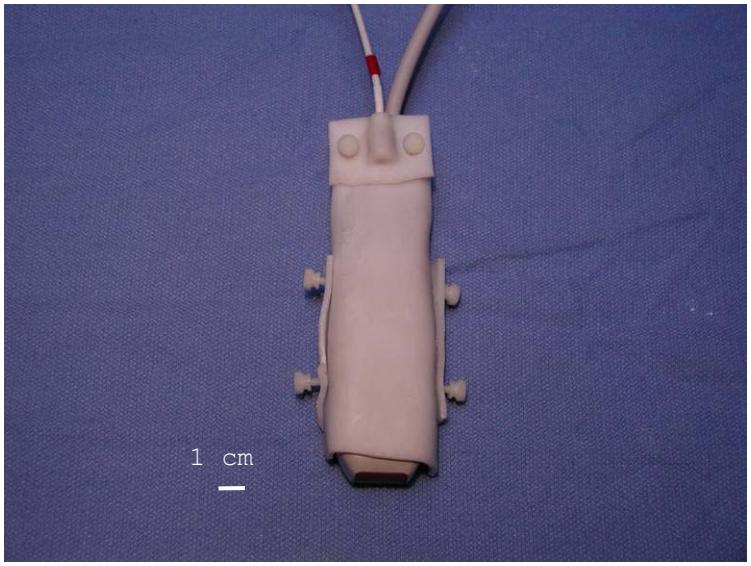

Figure 4.2 Tracking device attached to the US probe for generating spatially compounded US volumes.

much more obviously than in the maximum intensity method. In comparing both results for accuracy, the relevant anatomic landmarks can be seen in both; thus, the maximum intensity algorithm seems to hold important advantages of speed and a visually acceptable result for performing the final image assembly Figure 4.3. The steps taken to generate this composite volume are summarized in Figure 4.4. With integration of this process into the US platform, this entire series of steps could be performed in under fifteen minutes allowing six minutes for acquisition, six minutes to apply the transforms and then three additional minutes for assembly and display. Using a more current processor, this time could easily be reduced by a factor of four. Thus, this process could be performed in the operating room with the heart positioned as required for the surgical procedure.

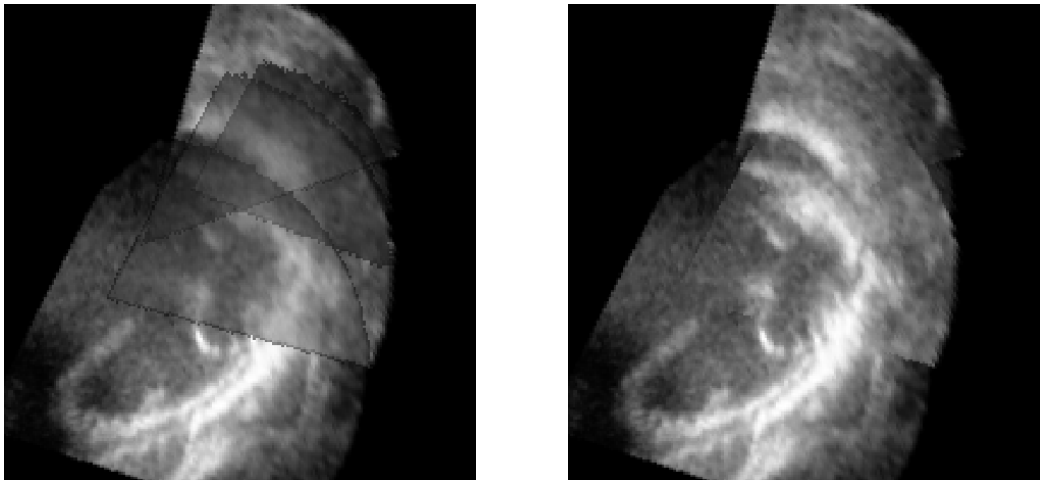

Figure 4.3 Comparison of weighted average spatial compounding (left) vs. maximum intensity spatial compounding (right).

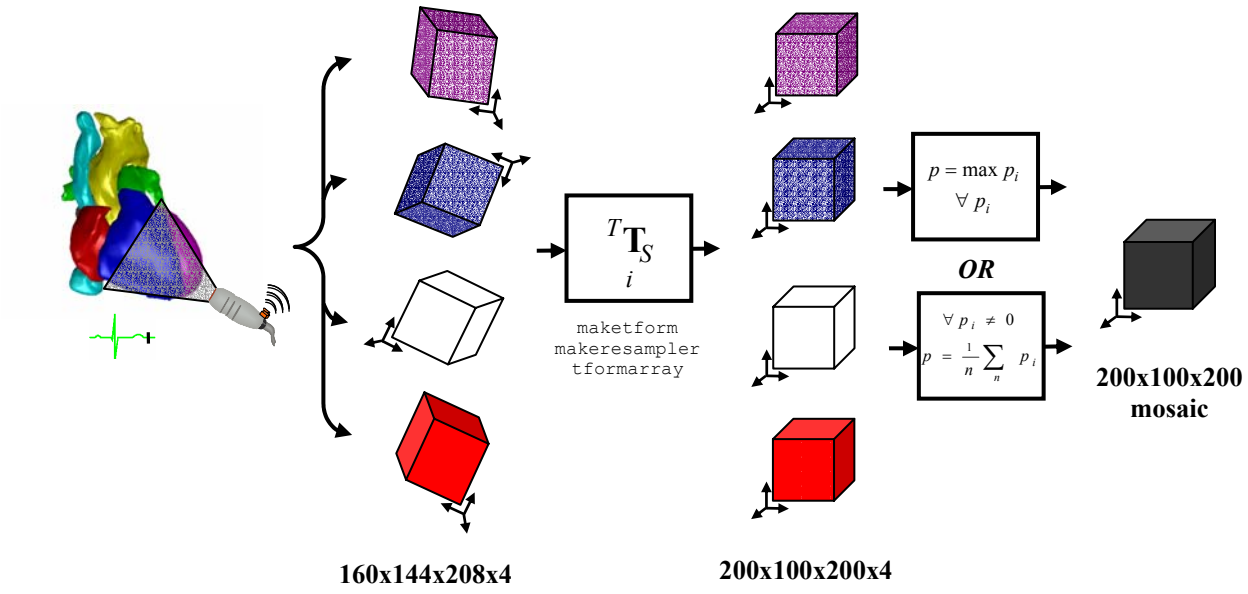

Figure 4.4 Flowchart illustrating the process used to create a composite US image volume using spatial compounding

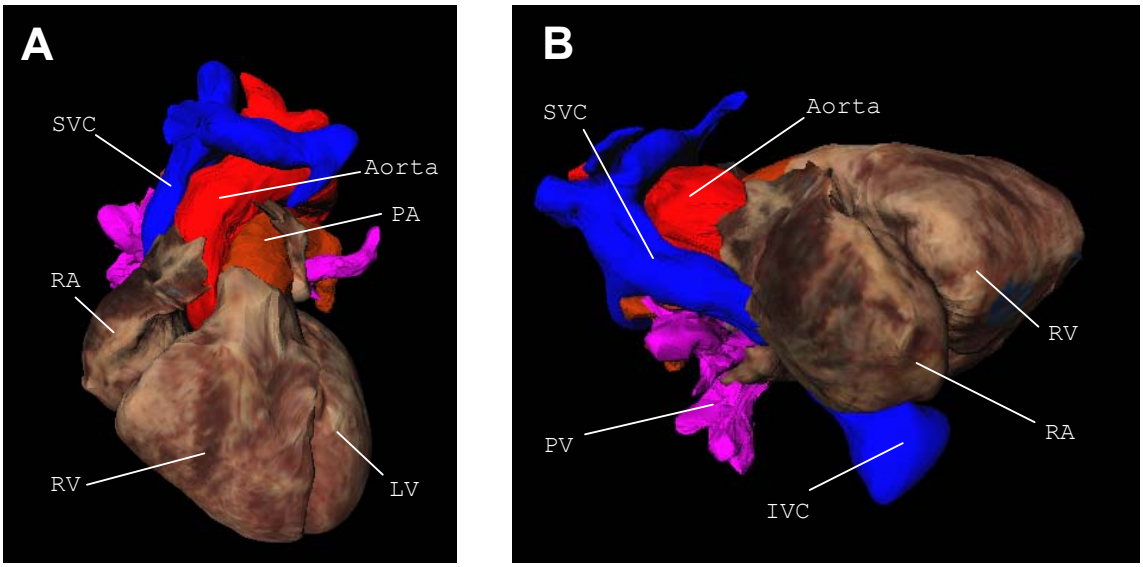

Figure 4.5 Original open-source VRML surface model of the human heart created from the Visible Human data set by Dr. Frank Sachse (Karlsruhe, Germany).

4.3 Model Generation

The heart model used for this project is based on the anatomic features of a normal adult female. The original data set for this model comes from the National Library of Medicine Visible Human Project which consists of both multi-modal imaging studies and fine anatomic cross sections of both an adult male and an adult female. Using the anatomic images from the Visible Female spaced at 0.33 mm, Sachse used deformable surface nets to create a detailed open source Virtual Reality Modeling Language (VRML) model of the human heart [88, 89].

This polygonal mesh surface model of the heart consists of sixteen modular sections comprised of approximately 10,000 vertices and 20,000 polygons each (Figure 4.5). For this thesis, each of the model sections was ported into MATLAB, formed into a `patch` object, and downsampled by 90% to speed rendering using the topology-preserving function `reducepatch`. This process is illustrated in Figure 4.6 demonstrating that this downsampling process does not sacrifice important anatomic detail.

To facilitate control point identification by taking advantage of the modular nature of this model, a user interface tool was designed to display the current model both in cross section and as a polygonal mesh surface. As an example of the functionality of this tool, Figure 4.7 illustrates the steps used to identify the midpoint of the posterior mitral valve annulus (support structure for the valve). 1) Load the default model into the interface which presents the four heart chambers. 2) Remove unnecessary

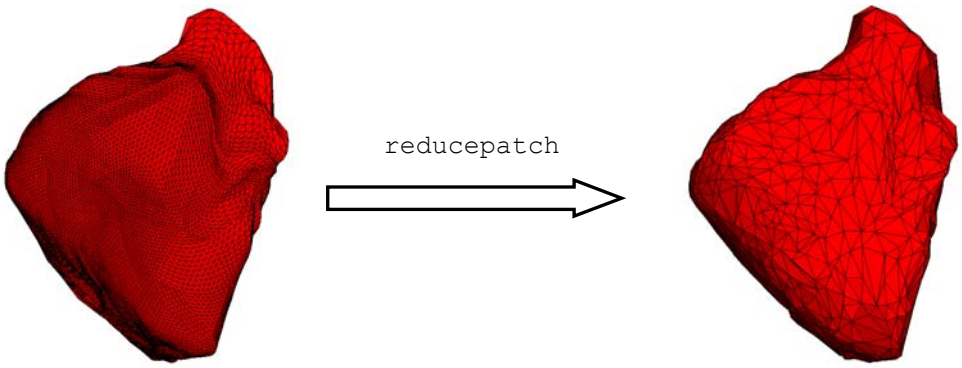

Figure 4.6 Illustration of the ported VRML model (only the right ventricle is shown) as a MATLAB `patch` object which is then downsampled by 90% to reduce rendering overhead without sacrificing significant anatomic detail.

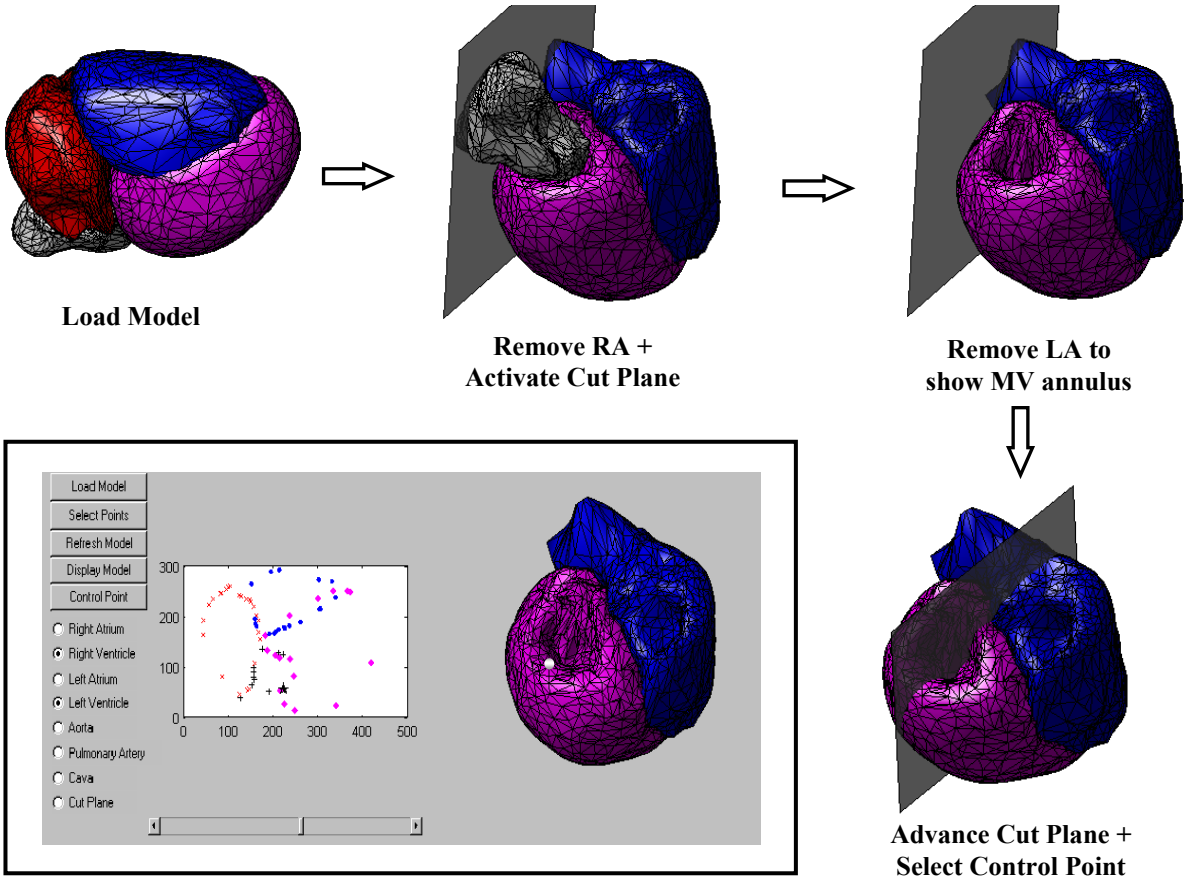

Figure 4.7 Flowchart illustrating the process of control point selection within the graphical model.

model parts such as the right atrium. Rotate the model so that the region of the mitral valve can be seen and activate the cut plane. This cut plane shows the vertices along this cut surface as a cross section of the model displayed in the middle window. 3) Move the cut plane to the region of the mitral valve and then de-activate the Left Atrium radio button. 4) Refresh the model view and then rotate the model to view the depression that represents the mitral valve. Continue advancing the cut plane to the lateral wall of the ventricle and then select the appropriate control point within the cross-section display window.

4.4 Model Matching

The final step in this process involves transforming the graphical model so that the anatomic structures of the model accurately represents the corresponding anatomic features of the patient. Once this has been accomplished, the surgical tools can be animated within this model as an accessory navigational aid even as the real time 3-D US images the surgical target.

4.4.1 Registration

For speed and simplicity, a least squares method was used to infer the nonrigid transform matrix between the US and model control point pairs. Given n control point pairs, a matrix of homogenous vectors can be formed for both the model control points, $\mathbf{M}$ and the US image control points, $\mathbf{U}$. Thus, the goal is to solve for the homogeneous non-rigid transform matrix, ${}^{U}\mathbf{T}_{M}$ which maps points in $\mathbf{M}$ to points in $\mathbf{U}$:

$$ {}^{U}\mathbf{T}_{M}\mathbf{M} = \mathbf{U} . \tag{4.1} $$

${}^{U}\mathbf{T}_{M} \in \mathbb{R}^{4x4}$ has the form of a general three dimensional transform matrix:

$$ \begin{bmatrix} a_{11} & a_{12} & a_{13} & d_x \\ a_{21} & a_{22} & a_{23} & d_y \\ a_{31} & a_{32} & a_{33} & d_z \\ 0 & 0 & 0 & 1 \end{bmatrix} \tag{4.2} $$

while $\mathbf{M}$ and $\mathbf{U}$ are matrices of columns in the form

$$ \mathbf{M} = \left[\begin{array}{c|c|c|c} & & & \\ m_1 & m_2 & \cdots & m_n \\ & & & \end{array} \right] \tag{4.3} $$

and

$$\mathbf{U} = \left[\begin{array}{c|c|c|c} u_1 & u_2 & \cdots & u_n \end{array}\right]. \tag{4.4}$$

Each of these n columns is a homogeneous position vector such as

$$m_n = \begin{bmatrix} m_x \\ m_y \\ m_z \\ 1 \end{bmatrix}. \tag{4.5}$$

The normal equations represent the standard approach to solving least squares problems. The typical algorithm involves taking the Cholesky factorization which requires $\sim 4^3(n+\frac{4}{3})$ flops for the problem described here. In this case, the computational expense scales linearly as the number of control points n increases. Although asymptotically this algorithm only requires half as many flops as most such algorithms for matrices where $i \gg j$, the this approach is an inherently unstable method for solving least squares problems [90]. Thus, for this model matching problem, a more suitable result is achieved by using reduced QR factorization by Householder triangularization. The expense of this approach is only $\sim 4^3(2n-\frac{8}{3})$ flops which for $n=10$ takes only 0.4 sec on a 1 GHz laptop computer.

The MATLAB backslash operator \ uses Householder triangularization to solve least squares problems. Thus, by forming control point pairs from the model and the US volume into $\mathbf{M}$ and $\mathbf{U}$, respectively as in (4.3) and (4.4), the following lines of code solve for the matrix ${}^{U}\mathbf{T}_{M}$:

```
T=M'\U';

T=T';
```

4.4.2 Validation

Although visual inspection sometimes serves as the validation measure when registering graphical models to medical images [91, 92], quantitative validation is required before considering a technique acceptable for clinical use [93]. Thus, for this work, the accuracy of the registration process was quantified using several measures. First, a direct measure of the goodness of fit is given by the norm of the residual at each control point. However, these values do not give any indication of the quality of fit between the complete heart structures in the model and the image.

To assess the global registration result, matches between both structure centroids and surfaces were compared. To find the centroid of structures of interest in the US image, the manual segmentation tool described previously was used to generate a volumetric binary image of the

structure. The center of mass of this binary structure can then be determined using the `regionprops` function in the MATLAB Image Processing Toolbox. For the anatomic models, a vertex-based binary image was generated for each structure of interest. This was performed directly for the heart chambers and by manually selecting vertices of interest for the valves. Because the walls of the ventricular chambers were not well visualized in all parts of the US image, this analysis was restricted to the atria which were both fully seen and the most prominent valves within the image (MV and AV in this case).

A simple surface-based matching algorithm was also used to determine the goodness of fit within each image slice. Although this is only 2-D, it provides a general indication of the fit quality which can be interpreted in the context of the previous measures which are inherently 3-D. This assessment was performed by manually selecting model vertices corresponding to an anatomic feature within the US image. A cubic spline was then interpolated between these vertices. Subsequently, the corresponding structure was segmented from the US image using the same number of control points as vertices. A spline with the same sampling density was then interpolated between the image-based control points. This process establishes homology between points along the interpolated curves. These homologous points were then analyzed with the following measures:

$$E_{mean} = \frac{1}{n}\sum_{i=1}^{n}\left\|m_i - u_i\right\|_2 \tag{4.6}$$

$$E_{\max} = \max_{i=1,n}\left\|m_i - u_i\right\|_2 \tag{4.7}$$

where m_i and u_i are control point pairs in the model and US image, respectively.

Finally, morphological differences between models can be assessed by examining the condition number, $\kappa(\mathbf{T})$ of the transform matrix used to generate each model. As the ratio between the largest and smallest singular values of a matrix, this number indicated the map of a unit hypersphere in *n*-dimensional space under the *n* x *n* matrix. A very large condition number indicates a highly eccentric map under the action of this matrix which is ill-conditioned.

4.5 Results

Initially, six control point pairs were identified in the composite US volume and the graphical model. This is the minimum number of data points required to constrain the problem outlined above. The anatomic landmarks for these points included the apex of the heart, the lateral leaflet of the tricuspid valve, the posterior leaflet of the mitral valve, and the anterior and posterior aspects of the aortic valve and the anterior aspect of the pulmonic valve. The resulting transform matrix ${}^{U}\mathbf{T}_{M}$ was then applied to the graphical model. Validation then included slice-by-slice visual inspection (Figure 4.8), volumetric

visualization of the transformed model imbedded within the US volume (Figure 4.9), and use of all three quantitative measures described above.

With these six control points, the heart model was scaled, translated and rotated in a way that preserved the anatomic morphology of the model. In the slice-by-slice examination, the fit appeared acceptible in the area of the atrial chambers. The ventricular chambers also showed that the vertices of

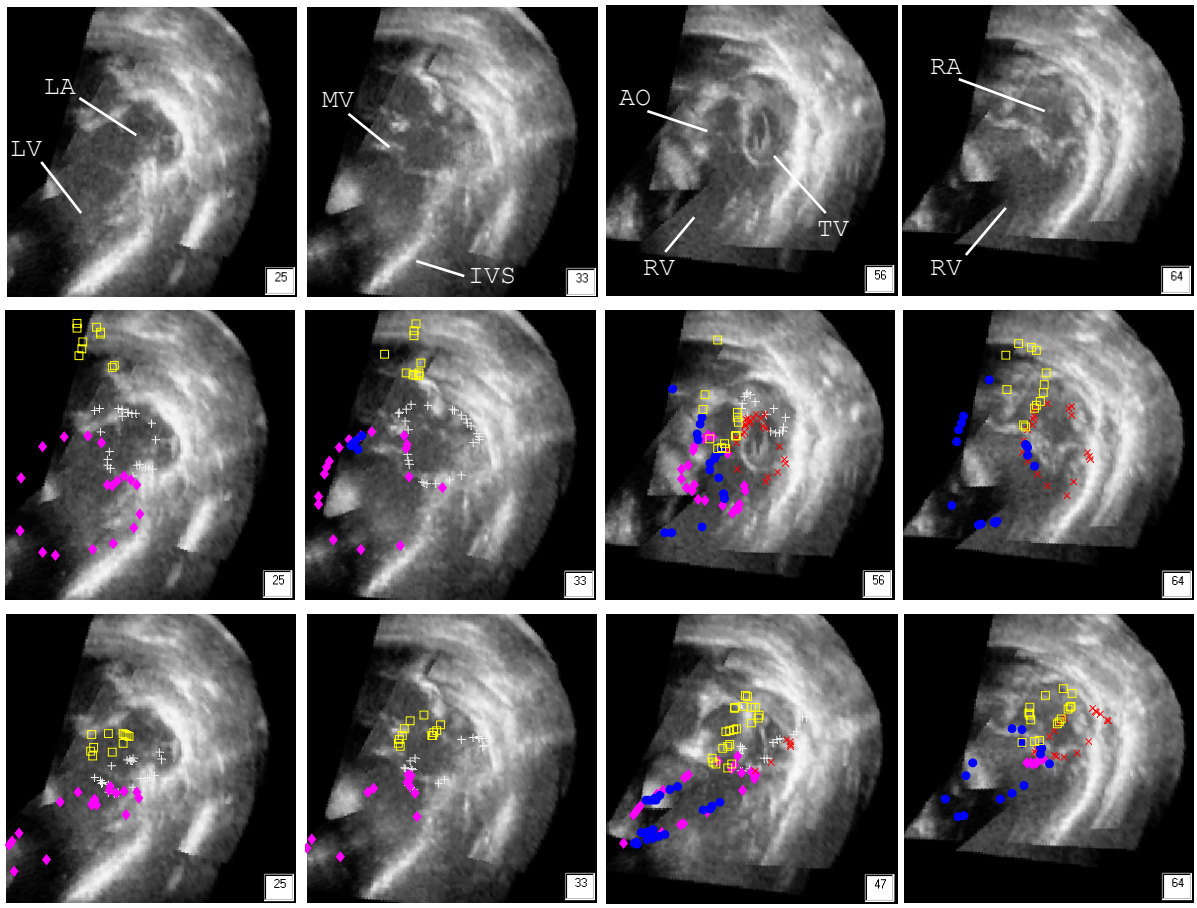

Figure 4.8 Goodness of fit assessment using cross-section matching. Top row shows four representative slices panning through the heart image from left to right with anatomic features noted. Middle row, n=6 control point pairs; Bottom row, n=10 control point pairs. + = LA = left atrium; ♦ = LV = left ventricle; × = RA = right atrium; ● = RV = right ventricle; ■ = AO = aorta; MV = mitral valve; IVS = interventricular septum; TV = Tricuspid valve

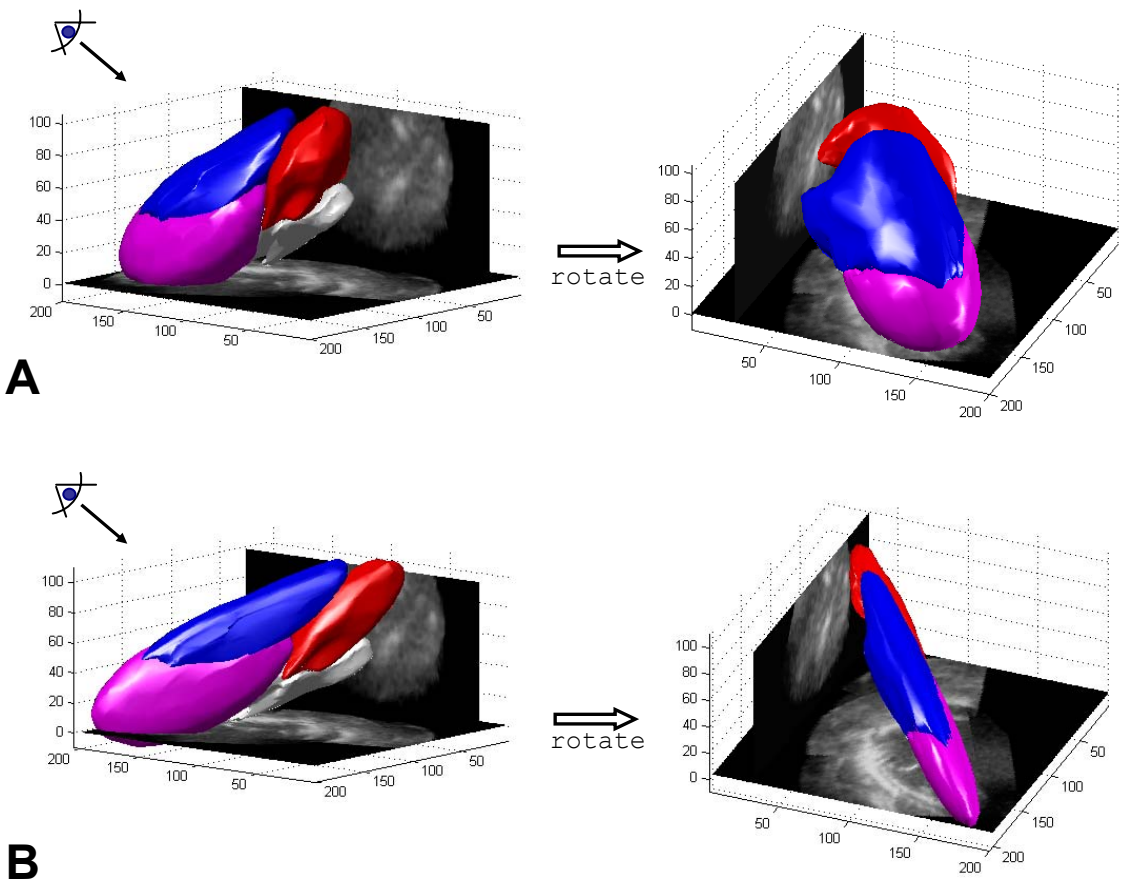

Figure 4.9 Results for model matching using least squares registration of paired control points. A) Shows two views of the match obtained with six control points. B) Additional control points for a total of ten resulted in significant compression along the anterior-posterior direction as seen in the second view.

Table 4.1 Summary of Control Points and Least Squares Residuals

	Norm of the Residual (mm)	
Control Point	***n*=6**	***n*=10**
Ventricular Apex	0.9	11.8
Anterior Aortic Valve	9.4	9.4
Posterior Aortic Valve	18.1	11.1
Anterior Mitral Valve	16.4	10.8
Posterior Mitral Valve	4.9	10.8
Antero-Lateral Tricuspid Valve	8.3	7.0
LV Lateral Wall-Posterior 1		3.3
LV Lateral Wall-Posterior 2		3.2
LV Wall-Anterior 1		1.5
LV Wall-Anterior 2		3.7
Mean ± SEM	**9.7±2.7**	**5.7±1.8**

the model components were positioned anatomically correctly in the vicinity of the corresponding structures within the US image (Top and middle row of Figure 4.8 and . Figure 4.9A).

For comparison and in an attempt to improve the overall fit, addition control points were selected in both the US image and the heart model. These points were selected along the anterior and posterior wall of the LV including the posterior papillary muscle as these were the only additional features that could be identified. The results of this fit are shown in the bottom of Figure 4.8 and in Figure 4.9B. These illustrations show that these additional points altered the overall morpholgy of the heart by compressing it in the anterior-posterior direction.

Table 4.2 Euclidean Distance Between Centroid in US & Model

Structure	*n*=6	*n*=10
Left Atrium	23.6 mm	15.8 mm
Right Atrium	22.9	26.7
Mitral Valve	10.5	14.5
Aortic Valve	10.8	3.8
Mean±SEM	**16.9±3.6**	**15.2±4.7**

Table 4.3 Maximum and Mean Error for Matching Surfaces

	E_{mean} (mm)		E_{max} (mm)	
Structure/Slice #	***n*=6**	***n*=6**	***n*=6**	***n*=6**
LV Wall				
1	11.1	26.2	23.1	32.6
7	20.3	12.6	24.8	19.9
13	13.5	15.1	20.4	18.3
RMS	15.5	**18.9**	22.8	**24.5**
LA Wall				
19	2.7	15.5	6.5	24.3
30	4.2	10.8	7.4	14.4
RMS	3.5	**13.4**	7.0	**20.0**
RA Wall				
53	18.6	5.0	23.7	8.1
65	27.7	12.0	38.1	17.6
RMS	**23.6**	9.2	**31.7**	13.7
Aortic Valve				
45	5.5	7.1	8.6	8.2
57	2.8	8.4	4.1	11.0
RMS	4.4	**7.8**	6.7	**9.7**

Table 4.4 Transform Matrices with Associated Condition Numbers

	***n*=6**	***n*=10**
${}^{U}\mathbf{T}_{M}$	$\begin{bmatrix} 0.285 & 0.135 & -0.121 & 84.3 \\ 0.186 & -0.164 & 0.249 & 5.43 \\ -0.213 & 0.236 & 0.126 & 18.2 \\ 0 & 0 & 0 & 1 \end{bmatrix}$	$\begin{bmatrix} 0.379 & 0.058 & -0.124 & 70.1 \\ 0.333 & -0.157 & 0.010 & 55.6 \\ -0.208 & 0.261 & 0.123 & 17.3 \\ 0 & 0 & 0 & 1 \end{bmatrix}$
$\kappa(\mathbf{T})$	$\mathbf{2.7x10^4}$	$\mathbf{3.1x10^4}$

Tables 4.1-3 summarize the quantitative validation performed on these two transformed models. With additional control points, the average norm of the residuals decreased from 9.7±2.7 mm to 5.7±1.8 mm. However, when evaluating the fit as a whole, the results were comparable for both models. The mean distance between centroids for four heart structures was over 15 mm in both cases. (Table 4.2). The magnitude of this error was borne out in the surface matching analysis (Table 4.3). This assessment showed a maximum error of up to 38.1 mm in the first model (*n*=6) and up to 32.6 mm in the latter model (*n*=10). Of the four structures examined, the latter model showed a greater RMS error in three (LV Wall, LA Wall, and Aortic Valve) indicating no benefit from the added control points.

The condition numbers of these two matrices is on the same order of magnitude. Furthermore, these numbers are relatively small. Thus, these matrices are not ill-conditioned, and the morphological differences between the models is only partly explained by the greater eccentricity of the singular values in the model for *n*=10.

4.6 Discussion

The inability to quickly and accurately re-position surgical instruments within the imaging field represents a significant limitation to using US imaging to guide procedures. Thus, a navigational aid has been developed to facilitate surgeon orientation relative to the important heart structures even when the instruments are outside the immediate field of view. Implementation of this navigational aid involves a two-step process. First, anatomic landmarks are identified within a spatially compounded US image of the heart. Then a graphical model of the heart is registered to these landmarks by selecting matching control points within the heart model.

This model registration approach was chosen over complete segmentation of the heart from the image data set for several reasons. First, the quality of the mosaic images was unknown at the start of this project. Although spatial compounding can potentially reduce noise within the US image, the semi-automatic segmentation algorithm employed in this study requires the heart wall to be completely or nearly completely visible in each image slice. Furthermore, by using a combination of image processing techniques (i.e. segmentation for virtual fixtures and model matching for orientation), the reliability of the overall system is potentially increased.

For clinical use, 3 mm registration accuracy is considered standard [85]. Thus, the approach described here requires improvements or implementation of alternative techniques to achieve the goal of an accurate navigational based on image data or other positional information which can be collected at the time of surgery. The major limitations of the model matching approach include the complete reliance on the expertise of the user to select matching points in two different 3-D volumes and the sensitivity of the least squares registration process to slight errors in this control point selection process. Following the spatial compounding process, the orientation of the original images has completely changed. Thus, the user must try to understand the structures within the image based on their orientation to one another with no ability to reference back to the original acquisition process to put the images in context. Depending on the experience of the user and the quality of the final image, this process can take several minutes and may require multiple reviews by the user to ensure an accurate interpretation. One approach to solving this limitation is to allow the user to select control points within rendered volume using an arbitrary cut plane. This approach would also limit many of the errors in control point correspondence which lead to a poor fit as seen in the second result demonstrated above.

Because the heart is a nonrigid, moving structure, elastic registration is ideally required for an optimal fit [93]. However, the computational expense of finding a true global minimum for the registration cost function often proves excessive. Furthermore, the limited number of internal landmarks and the susceptibility of these landmarks to change with various diseases can limit the accuracy of a point-based registration approach [92]. Surface-based registration may work well in this case where the US image is being registered to a surface model of the heart [93] (and the references therein). Promising results have also been achieved using a more computationally complete algorithm based on matching organ shape deformation modes [94]. Drawbacks of this approach include high computation requirements and the need to segment the initial image to obtain the base model to which the graphical mesh model is registered.

4.7 Conclusions

Enabling the surgeon to maintain orientation at all times throughout an image-guided procedure represents an important step towards making these procedures both safe and efficient. The technique described here represents an initial approach to this problem using spatial compounding and atlas-based model matching to produce a registered navigational aid for the surgeon. Although gross matching of heart structures was successfully performed using a landmark-based registration process, the accuracy of this registration falls below that required for clinical use. Future approaches could include surface-based registration or complete segmentation of the composite US image or perhaps navigational aids based solely on tracker data to complement the real time US imaging in guiding these procedures.

5 Contributions and Conclusions

DEVELOPING methods for using real time 3-D US for guiding surgery inside the beating heart represents the primary focus of this thesis. This chapter summarizes the principal contributions of this work and discusses possible directions for future research.

5.1 Primary Contributions

The work performed for this thesis has resulted in the conclusive demonstration of the superiority of real time 3-D US for guiding surgical procedures in cases where optical imaging is not available, the establishment of a viable animal model for exploring the possibility of performing surgery inside a beating heart using 3-D US for image guidance, and the development of several software tools for use during these procedures. This work represents the early efforts to both identify the limitations to using real time acoustic imaging for image guided procedures and to develop specific solutions addressing these limitations. Thus, the primary contributions of this thesis can be divided into 1) findings from initial tests both *in vivo* and *in vitro* using real time 3-D US for guiding surgical tasks and 2) solutions to problems identified during these initial studies. These contributions are summarized in Figure 5.1.

5.1.1 Initial studies using real time 3-D US to guide surgical procedures

At the beginning of this work, volumetric *real time* 3-D US had not been implemented as a viable tool for guiding surgical interventions. With the development of a 2-D phased array for acquiring acoustic images in real time, the tedious and time-consuming offline work to assemble multiple 2-D slices into a composite volume was effectively eliminated. Furthermore, applications for this imaging modality to more than just diagnosis were immediately apparent. Thus, in this work, we sought to begin to explore the possibility of developing real time 3-D US as an interventional tool. The specific applications motivating this work were derived from beating heart intracardiac surgery with the goal of eliminating the need for cardiopulmonary bypass and eventually the need for large incisions. However, use of real

time 3-D US for image-guided surgical interventions can extend to almost any surgical field including neurosurgery, urology, general surgery involving solid organs such as the liver and breast, and *in utero* fetal surgery.

The *in vitro* tank study performed early in this work showed that in cases where either direct visualization or endoscopic optical imaging is not available, real time 3-D US is a viable method for guiding even complex surgical maneuvers. For even the most basic tasks, real time 3-D US proved

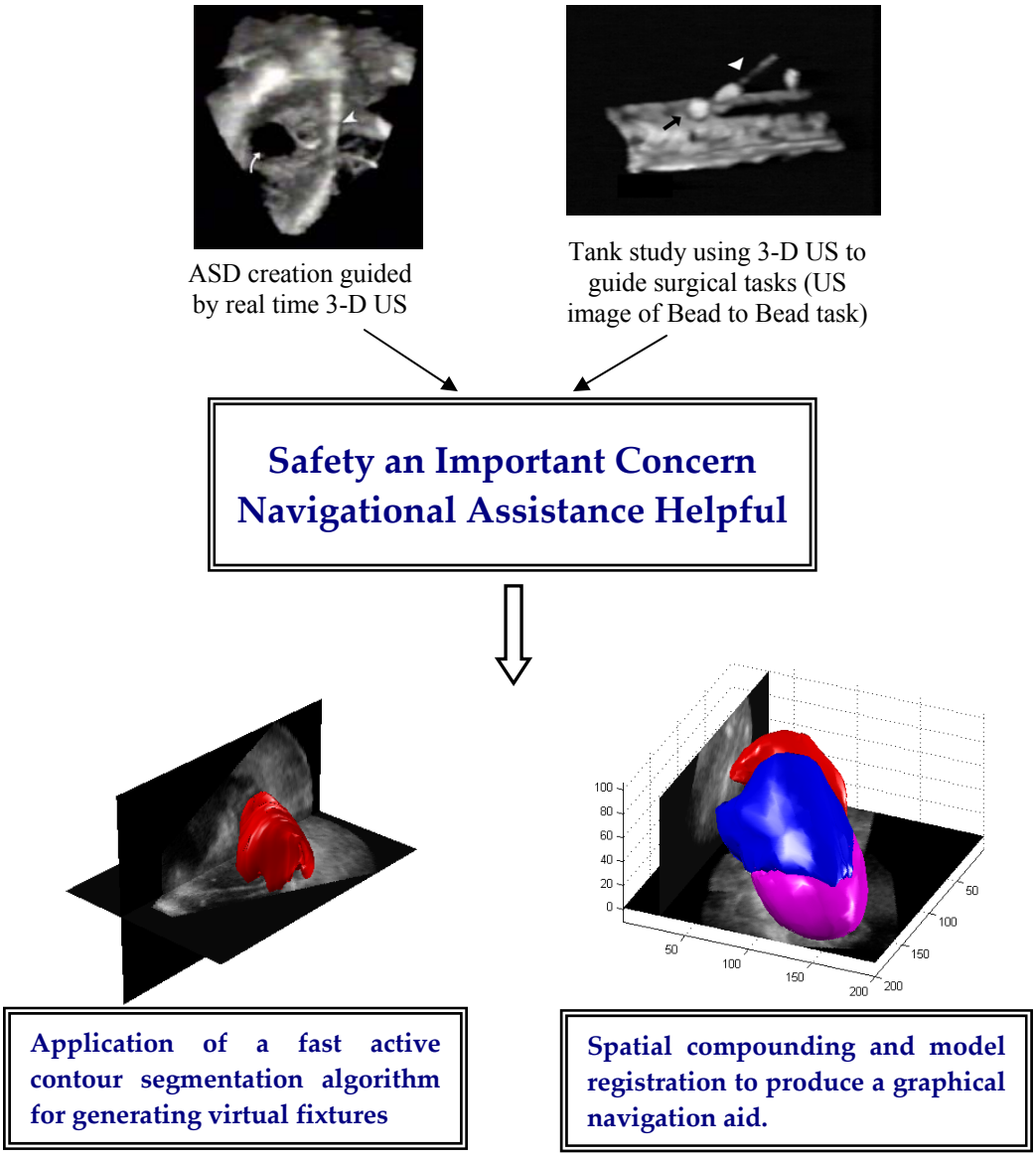

Figure 5.1. Summary of thesis contributions. These include feasibility assessment for using real time 3-D US to guide surgical procedures. This assessment revealed the specific need for additional safety measures and navigational assistance to help position instruments within the imaging field of view. The former need was addressed by applying an efficient algorithm for image segmentation using active contours while spatial compounding and model registration were implemented as a navigational aid.

superior to 2-D US imaging. Furthermore, 3-D US permitted the completion of a 2-instrument task which was not possible with 2-D US alone. Furthermore, trajectory analysis during one of the basic navigation tasks allowed quantification of the differences in performance when using 2-D US vs. 3-D US during these procedures.

The primary challenge identified during this study (noted by four of seven participants) involved the relatively small field of view and the difficulty getting the instrument back into the field of view following accidental excursions. This seemed to be less of a problem when the surgeon held the US probe while performing a simple one-instrument navigation task although this advantage did not lead to statistically significant performance improvements. Furthermore, this approach is not viable for most surgical procedures requiring the simultaneous use of two instruments.

The other aspect of these preliminary investigations included a series of animal experiments designed to further evaluate the possibility of performing image-guided surgical procedures inside a beating heart. These experiments also showed the inadequacy of 2-D US for guiding surgical tasks where out-of-plane movements are required. The issue of safety also became very clearly important with two inadvertent injuries sustained during these procedures with such a narrow margin of error. As in the tank study, while using 3-D US, macroscopic orientation and navigation into the field of view proved an important problem. Finally, the use of an auxiliary frame of reference in the form of a registered graphical model indicated the possible use of this kind of approach for addressing the issue of surgeon orientation.

5.1.2 Solutions to identified problems

In these initial studies, the issues of procedure safety and surgeon orientation emerged as the most important potential limitations for ensuring a safe, reliable, and efficient approach to image-guided surgery inside a beating heart. Developing solutions to these two issues led to the creation of several software tools including a segmentation tool for both manual and semi-automatic segmentation and a model matching tool for registering a graphical model of the heart to a spatially compounded composite US image of the heart. All of these tools are currently implemented in MATLAB which makes these tools both easy to use and easy to modify as required.

Manual segmentation has an important role in the application of real time 3-D US to image-guided interventions. This includes scaling factor determination, control point selection, and validation of other segmentation techniques. Thus a manual segmentation tool was developed for this work and its use demonstrated in this thesis.

The primary image processing technique used for this work was active contour segmentation, and one of several possible applications of this approach is to generate a graphical (and eventually a physical) boundary to prevent inadvertent excursions outside the surgical field. The recent report of a fast and efficient snake deformable model by Perrin [52, 53] led to the implementation of this algorithm for use in these procedures. The speed and accuracy of this approach suggests the immediate possibility of updating an accurate "virtual fixture" inside the heart wall to prevent inadvertent injuries. Other applications for this approach include quantitative echocardiography to determine global cardiac function in real time [95], and identifying surgical tools inside the image volume [96].

To address the problem of surgeon orientation and difficulties navigating surgical instruments into the imaging field of view, a navigational aid was developed in the form of a registered graphical model. Implementing this solution involved multiple steps including 1) creation of a composite US volume using spatial compounding, 2) using this composite US volume containing all the relevant internal anatomic landmarks to identify registration control points 3) modification of an open-source graphical model with the proper balance of anatomic detail and fast rendering, 4) development of an interface tool for selecting matching control points within this model, 5) inferring a general 3-D transform matrix from the least squares fit between these control point pairs, and 6) assessing the goodness of fit between the graphical model and the original US landmarks. With the tools designed as part of this thesis, each of these steps requires at most a couple of minutes permitting the use of this approach at the time of surgery where long delays cannot be tolerated.

In summary, this thesis explored the use of real time 3-D US for guiding surgical procedures. Several important limitations to the broad use of this technology as an interventional tool were identified and solutions where designed and implemented. These solutions include the use of active contour segmentation which can keep pace with the streaming volumetric image for establishing a safety barrier inside the heart and a registered graphical model of the heart as a navigational aid for the surgeon. Both of these solutions include some form of an interactive model which augments the information contained within the displayed US image.

5.2 Suggestions for future work

Areas where this work can be extended range from systems integration and testing to addressing fundamental challenges with using deformable models for segmentation. This section highlights several points where more development work is required to make full implementation of 3-D US as an interventional tool a clinical reality.

Systems Integration

All of the tools developed in this thesis require to save the image file onto a CD, take the image file off the CD and port it from the raw image format (DICOM) into a 3-D array of intensity values which can then be read by the MATLAB tools developed here. Obviously, this approach obviates any sort of real-time interactive image processing on the image displayed by the US system. Thus, one of the first steps required to implement and validate the measures detailed here is to begin a full systems integration where the researcher has full access to the imaging PC. With this access, online image processing and manipulation can be performed using either the imaging PC or a separate external PC networked to the US system. Once this access is established, the range of potential investigations will significantly increase including the production of augmented US images as depicted in Figure 5.2.

Testing the tools developed in this work on an integrated system could be performed using an external networked PC. However, bandwidth limitations and computational overhead in MATLAB could lead to significant lag times which would limit the use of the real time segmentation tool, for example. For the tools which absolutely must work in real time (i.e. 20-25 volumes per second), these should be translated to C or C++ and run directly on the imaging PC if there is sufficient memory and processor time available. With this level of integration, other imaging techniques for increased spatial awareness such as stereo imaging or image oscillation could be readily implemented.

For the tools and applications which do not require real time processing, one logical step to making these tools more general would be the use of a scripting language such at TCL/TK for the user

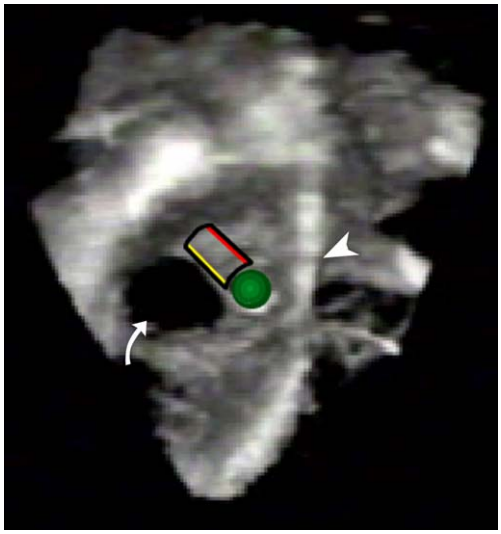

Figure 5.2 Augmented US image showing a the tool tip as it advances towards the atrial septum.

interfaces. The advantages of this approach include continued ease of use for the programmer as well as full access to the visualization toolkit (VTK; Kitware, Inc., Clifton Park, NY) and Insight Segmentation and Registration Toolkit (ITK; http://www.itk.org) libraries which are specifically designed for fast, efficient graphically enhanced medical imaging applications such as those discussed in this thesis.

Finally, full access to the streaming image data would enable the integration of other control systems for performing these surgical tasks. The use of surgical robotic tools represents an exciting area of new research [97] which may have important applications for surgery inside the heart [5, 8, 59]. Using images to guide robotic arms and instruments—visual servoing—also represents an area of research [65], [98] which when applied to heart surgery could enhance both the safety and efficiency of image-guided procedures. Specifically, the post-segmentation data which includes the inner surface of the heart could be specified as a "no fly zone" for the robotic arm thereby completely eliminating the possibility of the user inadvertently passing an instrument into other surrounding structures such as the heart wall or the aorta.

Image Processing Challenges

Another part of this project replete with research-oriented challenges lies in the difficulty of using acoustic imaging as the primary imaging modality. Currently, MRI represents the most viable alternative to this imaging approach [32]; however, the temporal resolution and the cumbersome nature of the "open MRI" setup make US imaging much more attractive for guiding intracardiac procedures. Thus, any progress that can be made in the quality of the acoustic image such as improving the signal to noise ratio, appropriately adjusting the many controls such as system gain and transmit power, and understanding the process of artifact generation from tool surfaces will serve to further enhance the utility of this imaging modality for guiding interventions.

Another challenge lies in accurate segmentation of these acoustic images. The algorithm used in this thesis performs reasonably well once the user becomes familiar with the range of appropriate settings for the control parameters β, ρ, and k. However, this segmentation approach requires that the image of the heart walls or other structure of interest be relatively intact. Problems of signal dropout lead to erroneous results which have motivated numerous algorithmic fixes [99]. The most straightforward approach for future intracardiac procedures is to perform these procedures while infusing a small amount of US contrast into the bloodstream. These contrast agents contain stabilized microbubbles of harmless gas such as carbon dioxide which give a bright acoustic signal. This would facilitate rapid segmentation of the heart chambers if required during surgical interventions.

Finally, the need to form a composite US image for model registration could be eliminated by expanding the capabilities of the "full volume" mode in the current US system. This would permit the addition of additional volumes into this data set using beam steering instead of tracking the US probe. However, the technique employed in this study does have more general uses especially when performing procedures inside much larger organs such as the liver or kidney. Thus, one solution would be to allow the user to select the appropriate method for spatial compounding with each procedure. In the case of matching multiple arbitrarily oriented volumes, additional measures could be taken to improve the appearance of the image and to eliminate artifacts. In this thesis, no additional intensity-based registration was performed after the initial fit was obtained using the EM tracking data by using an EKG-gated imaging and breath holding to minimize motion artifact during acquisition. This US-US registration problem includes two main challenges: limiting the search space so that the computation time is reasonable and determining the appropriate transform to improve the match between adjacent volumes. One idea for limiting the search space during this volumetric US-US registration problem is to use the EM tracker to not only perform the initial registration but also to determine the location of the "seams" between adjacent volumes. Thus, within each region of overlap, one could further reduce the search space by looking only at a narrow band of pixels at the junction between one volume and the other. Performing the actual fit between volumes represents a rich field of active research [84, 87]. Because correlation-based techniques prove sensitive to image artifacts and system setting changes, probabilistic methods such as mutual information [100, 101] applied to the limited volume "seam" search space would likely prove more robust.

Contributions and Conclusions

Bibliography

[1] http://www.cardiovasculardocs.com.

[2] M. E. Brickner, L. D. Hillis, and R. A. Lange, "Congenital heart disease in adults. First of two parts," *N Engl J Med*, vol. 342, pp. 256-63, 2000.

[3] D. P. Bichell, T. Geva, E. A. Bacha, J. E. Mayer, R. A. Jonas, and P. J. del Nido, "Minimal access approach for the repair of atrial septal defect: the initial 135 patients," *Ann Thorac Surg*, vol. 70, pp. 115-8, 2000.

[4] I. A. Nicholson, D. P. Bichell, E. A. Bacha, and P. J. del Nido, "Minimal sternotomy approach for congenital heart operations," *Ann Thorac Surg*, vol. 71, pp. 469-72, 2001.

[5] L. Torracca, G. Ismeno, and O. Alfieri, "Totally endoscopic computer-enhanced atrial septal defect closure in six patients," *Ann Thorac Surg*, vol. 72, pp. 1354-7, 2001.

[6] http://www.ctsnet.org.

[7] L. Aklog, D. H. Adams, G. S. Couper, R. Gobezie, S. Sears, and L. H. Cohn, "Techniques and results of direct-access minimally invasive mitral valve surgery: a paradigm for the future," *J Thorac Cardiovasc Surg*, vol. 116, pp. 705-15, 1998.

[8] J. E. Felger, W. R. Chitwood, Jr., L. W. Nifong, and D. Holbert, "Evolution of mitral valve surgery: toward a totally endoscopic approach," *Ann Thorac Surg*, vol. 72, pp. 1203-9, 2001.

[9] J. Gibbons, "Application of a mechanical heart-lung apparatus to cardiac surgery," *Minn Med*, pp. 171, 1954.

[10] D. A. Stump, N. A. Kon, A. T. Rogers, and J. W. Hammon, "Emboli and Neuropsychological Outcome Following Cardiopulmonary Bypass," *Echocardiography*, vol. 13, pp. 555-558, 1996.

[11] M. Antonelli, G. Testa, L. Tritapepe, R. R. D'Errico, D. Costa, L. Giovannelli, L. Riccioni, A. Gasparetto, and G. Catena, "IL-8, IL-6 and ICAM-1 in serum of paediatric patients undergoing cardiopulmonary bypass with and without cardiocirculatory arrest," *J Cardiovasc Surg (Torino)*, vol. 40, pp. 803-9, 1999.

[12] J. Sonntag, I. Dahnert, B. Stiller, R. Hetzer, and P. E. Lange, "Complement and contact activation during cardiovascular operations in infants," *Ann Thorac Surg*, vol. 65, pp. 525-31, 1998.

[13] A. Roth-Isigkeit, L. Hasselbach, E. Ocklitz, S. Bruckner, A. Ros, H. Gehring, P. Schmucker, L. Rink, and M. Seyfarth, "Inter-individual differences in cytokine release in patients undergoing cardiac surgery with cardiopulmonary bypass," *Clin Exp Immunol*, vol. 125, pp. 80-8, 2001.

[14] C. C. Menache, A. J. du Plessis, D. L. Wessel, R. A. Jonas, and J. W. Newburger, "Current incidence of acute neurologic complications after open- heart operations in children," *Annals of Thoracic Surgery*, vol. 73, pp. 1752-1758, 2002.

[15] J. J. O'Brien, J. Butterworth, J. W. Hammon, K. J. Morris, J. M. Phipps, and D. A. Stump, "Cerebral emboli during cardiac surgery in children," *Anesthesiology*, vol. 87, pp. 1063-9, 1997.

[16] W. S. Stoney, W. C. Alford, Jr., G. R. Burrus, D. M. Glassford, Jr., and C. S. Thomas, Jr., "Air embolism and other accidents using pump oxygenators," *Ann Thorac Surg*, vol. 29, pp. 336-40, 1980.

[17] M. Struber, J. T. Cremer, B. Gohrbandt, C. Hagl, M. Jankowski, B. Volker, H. Ruckoldt, M. Martin, and A. Haverich, "Human cytokine responses to coronary artery bypass grafting with and without cardiopulmonary bypass," *Ann Thorac Surg*, vol. 68, pp. 1330-5, 1999.

[18] G. Asimakopoulos, "Systemic inflammation and cardiac surgery: an update," *Perfusion*, vol. 16, pp. 353-60, 2001.

[19] D. Harken, L. Ellis, P. Ware, and L. Norman, "The surgical treatment of mitral stenosis. I. Valvuloplasty," *N Engl J Med*, vol. 239, pp. 801-9, 1948.

[20] C. Bailey, "The surgical treatment of mitral stenosis (mitral commissurotomy)," *Dis Chest*, vol. 15, pp. 377-97, 1949.

[21] R. Gross, E. J. Watkins, M. Pomeranz, and E. Godsmith, "Method for surgical closure of interauriclar septal defects," *Surg Gyn Obstet*, vol. 96, pp. 1, 1953.

[22] G. P. Fontana, "Minimally invasive cardiac surgery," *Chest Surg Clin N Am*, vol. 8, pp. 871-90, 1998.

[23] E. Buffolo, C. S. de Andrade, J. N. Branco, C. A. Teles, L. F. Aguiar, and W. J. Gomes, "Coronary artery bypass grafting without cardiopulmonary bypass," *Ann Thorac Surg*, vol. 61, pp. 63-6, 1996.

[24] J. D. Puskas, V. H. Thourani, J. J. Marshall, S. J. Dempsey, M. A. Steiner, B. H. Sammons, W. M. Brown, 3rd, J. P. Gott, W. S. Weintraub, and R. A. Guyton, "Clinical outcomes, angiographic patency, and resource utilization in 200 consecutive off-pump coronary bypass patients," *Ann Thorac Surg*, vol. 71, pp. 1477-83; discussion 1483-4, 2001.

[25] M. Sogawa, H. Moro, M. Tsuchida, M. Shinonaga, H. Ohzeki, and J. Hayashi, "Development of an endocardioscope for repair of an atrial septal defect in the beating heart," *ASAIO J*, vol. 45, pp. 90-3, 1999.

[26] S. W. Downing, W. A. Herzog, Jr., J. S. McLaughlin, and T. P. Gilbert, "Beating-heart mitral valve surgery: preliminary model and methodology," *J Thorac Cardiovasc Surg*, vol. 123, pp. 1141-6, 2002.

[27] Y. Suematsu, S. Takamoto, Y. Kaneko, T. Ohtsuka, H. Takayama, Y. Kotsuka, and A. Murakami, "Beating atrial septal defect closure monitored by epicardial real-time three-dimensional echocardiography without cardiopulmonary bypass," *Circulation*, vol. 107, pp. 785-90, 2003.

[28] T. M. Peters, "Image-guided surgery: from X-rays to virtual reality," *Comput Methods Biomech Biomed Engin*, vol. 4, pp. 27-57, 2000.

[29] G. Sakas, "Trends in medical imaging: from 2D to 3D," *Computers & Graphics-Uk*, vol. 26, pp. 577-587, 2002.

[30] J. Cox, *Montreal Medical Journal*, vol. 24, pp. 661-665, 1896.

[31] J. Kettenbach, D. F. Kacher, S. K. Koskinen, S. G. Silverman, A. Nabavi, D. Gering, C. M. Tempany, R. B. Schwartz, R. Kikinis, P. M. Black, and F. A. Jolesz, "Interventional and intraoperative magnetic resonance imaging," *Annu Rev Biomed Eng*, vol. 2, pp. 661-90, 2000.

[32] C. Rickers, M. Jerosch-Herold, X. Hu, N. Murthy, X. Wang, H. Kong, R. T. Seethamraju, J. Weil, and N. M. Wilke, "Magnetic resonance image-guided transcatheter closure of atrial septal defects," *Circulation*, vol. 107, pp. 132-8, 2003.

[33] J. McGahan, "Invasive ultrasound principles (biopsy, aspiration, and drainage)," in *Diagnostic Ultrasound: A Logical Approach*, J. McGahan and B. Goldberg, Eds. Philadelphia: Lippincott-Raven, 1998, pp. 39-75.

[34] P. N. Wells, "Current status and future technical advances of ultrasonic imaging," *IEEE Eng Med Biol Mag*, vol. 19, pp. 14-20, 2000.

[35] H. H. Holm and B. Skjoldbye, "Interventional ultrasound," *Ultrasound Med Biol*, vol. 22, pp. 773-89, 1996.

[36] C. Nolsoe, L. Nielsen, S. Torp-Pedersen, and H. H. Holm, "Major complications and deaths due to interventional ultrasonography: a review of 8000 cases," *J Clin Ultrasound*, vol. 18, pp. 179-84, 1990.

[37] J. Caspers, C. Reading, J. McGahan, and J. Charboneau, "Ultrasound-guided biopsy and drainage of the abdomen and pelvis," in *Diagnostic Ultrasound*, C. Rumack, S. Wilson, and J. Charboneau, Eds. Boston: Mosby, 1998, pp. 599-628.

[38] M. Rosenthal, A. State, J. Lee, G. Hirota, J. Ackerman, K. Keller, E. Pisano, M. Jiroutek, K. Muller, and H. Fuchs, "Augmented reality guidance for needle biopsies: a randomized, controlled trial in phantoms," in *MICCAI 2001*, vol. 2208, *LNCS*, W. Niessen and M. Viergever, Eds. Berlin: Springer-Verlag, 2001, pp. 240-248.

[39] G. Megali, O. Tonet, C. Stefanini, M. Boccadoro, V. Papaspyropoulos, L. Angelini, and P. Dario, "A computer-assisted robotic ultrasound-guided biopsy system for video-assisted surgery," in *MICCAI 2001*, vol. 2208, *LNCS*, W. Niessen and M. Viergever, Eds. Berlin: Springer-Verlag, 2001, pp. 343-50.

[40] P. Dario, M. C. Carrozza, M. Marcacci, S. D'Attanasio, B. Magnami, O. Tonet, and G. Megali, "A novel mechatronic tool for computer-assisted arthroscopy," *IEEE Trans Inf Technol Biomed*, vol. 4, pp. 15-29, 2000.

[41] J. Harness and M. Gittleman, "Breast ultrasound," in *Ultrasound in Surgical Practice*, J. Harness and D. Wisher, Eds. New York: Wiley-Liss, 2001, pp. 159-235.

[42] G. S. Rozycki, "Surgeon-performed ultrasound: its use in clinical practice," *Ann Surg*, vol. 228, pp. 16-28, 1998.

[43] A. Siperstein, "Invasive Ultrasonography," in *Ultrasound in Surgical Practice*, J. Harness and D. Wisher, Eds. New York: Wiley-Liss, 2001, pp. 143-58.

[44] T. Nelson, D. Downey, D. Pretorius, and A. Fenster, "Interventional applications," in *Three-Dimensional Ultrasound*. New York: Lippincott Williams & Wilkins, 1999, pp. 217-27.

[45] A. Fenster and D. B. Downey, "Three-dimensional ultrasound imaging," *Annu Rev Biomed Eng*, vol. 2, pp. 457-75, 2000.

[46] E. D. Light, R. E. Davidsen, J. O. Fiering, T. A. Hruschka, and S. W. Smith, "Progress in two-dimensional arrays for real-time volumetric imaging," *Ultrason Imaging*, vol. 20, pp. 1-15, 1998.

[47] R. E. Davidsen, J. A. Jensen, and S. W. Smith, "Two-dimensional random arrays for real time volumetric imaging," *Ultrason Imaging*, vol. 16, pp. 143-63, 1994.

[48] K. Shung and M. Zipparo, "Ultrasonic transducers and arrays," *IEEE Eng Med Biol Mag*, vol. 15, pp. 20-30, 1996.

[49] T. R. Nelson and D. H. Pretorius, "Three-dimensional ultrasound imaging," *Ultrasound Med Biol*, vol. 24, pp. 1243-70, 1998.

[50] R. E. Kardon, Q. L. Cao, N. Masani, L. Sugeng, S. Supran, K. G. Warner, N. G. Pandian, and G. R. Marx, "New insights and observations in three-dimensional echocardiographic visualization of ventricular septal defects: experimental and clinical studies," *Circulation*, vol. 98, pp. 1307-14, 1998.

[51] M. Vogel, S. Y. Ho, C. Lincoln, M. H. Yacoub, and R. H. Anderson, "Three-dimensional echocardiography can simulate intraoperative visualization of congenitally malformed hearts," *Ann Thorac Surg*, vol. 60, pp. 1282-8, 1995.

[52] D. Perrin, "Vision-based tasks and dynamic contours." Doctoral Thesis in the Department of Computer Science, University of Minnesota, 2002.

[53] D. Perrin and C. Smith, "Rethinking classical internal forces for active contour models," presented at CVPR, Kauai, HI, 2001.

[54] A. Watt and M. Watt, "Volume rendering techniques," in *Advanced animation and rendering techniques: theory and practice*, A. Watt and M. Watt, Eds. Reading, MA: Addison-Wesley, 1992, pp. 297-321.

[55] S. A. Ben-Haim, D. Osadchy, I. Schuster, L. Gepstein, G. Hayam, and M. E. Josephson, "Nonfluoroscopic, in vivo navigation and mapping technology," *Nat Med*, vol. 2, pp. 1393-5, 1996.

[56] G. Bolotin, T. Wolf, F. H. van der Veen, R. Shachner, Y. Sazbon, D. Reisfeld, R. Shofti, R. Lorusso, S. Ben-Haim, and G. Uretzky, "Three-dimensional electromechanical mapping: imaging in the operating room of the future," *Ann Thorac Surg*, vol. 72, pp. S1083-9, 2001.

[57] L. Gepstein, G. Hayam, and S. A. Ben-Haim, "A novel method for nonfluoroscopic catheter-based electroanatomical mapping of the heart. In vitro and in vivo accuracy results," *Circulation*, vol. 95, pp. 1611-22, 1997.

[58] T. Kohl, "Fetal echocardiography: new grounds to explore during fetal cardiac intervention," *Pediatr Cardiol*, vol. 23, pp. 334-46, 2002.

[59] J. W. Cannon, R. D. Howe, P. E. Dupont, J. K. Triedman, G. R. Marx, and P. J. del Nido, "Application of Robotics in Congenital Cardiac Surgery," *Semin Thorac Cardiovasc Surg: Pediatric Cardiac Surgery Annual*, In Press.

[60] L. Wanger, J. Ferwerda, and D. Greenberg, "Perceiving spatial relationships in computer-generated images," *IEEE Comput Graph Appl*, vol. 12, pp. 44-58, 1992.

[61] A. Tsai, "Curve evolution and estimation-theoretic techniques for image processing." Doctoral Thesis in Health Sciences and Technology, MIT, 2001.

[62] G. M. Treece, R. W. Prager, A. H. Gee, and L. Berman, "Surface interpolation from sparse cross sections using region correspondence," *IEEE Trans Med Imaging*, vol. 19, pp. 1106-14, 2000.

[63] T. McInerney and D. Terzopoulos, "Deformable models in medical image analysis: a survey," *Med. Image Anal,* vol. 1, pp. 91-108, 1996.

[64] G. Borgefors, "Distance Transformations in Digital Images," *Computer Vision Graphics and Image Processing*, vol. 34, pp. 344-371, 1986.

[65] J. Stoll, P. Dupont, and R. Howe, "Ultrasound-based Servoing of Manipulators for Telesurgery," presented at Telemanipulator and Telepresence Technologies VIII Conference, Newton, MA, 2001.

[66] I. Mikic, S. Krucinski, and J. D. Thomas, "Segmentation and tracking in echocardiographic sequences: Active contours guided by optical flow estimates," *IEEE Transactions on Medical Imaging*, vol. 17, pp. 274-284, 1998.

[67] M. Kass, A. Witkin, and D. Terzopoulos, "Snakes - Active Contour Models," *International Journal of Computer Vision*, vol. 1, pp. 321-331, 1987.

[68] O. Gerard, A. C. Billon, J. M. Rouet, M. Jacob, M. Fradkin, and C. Allouche, "Efficient model-based quantification of left ventricular function in 3-D echocardiography," *IEEE Transactions on Medical Imaging*, vol. 21, pp. 1059-1068, 2002.

[69] R. Malladi and J. Sethian, "Level Set Methods for Curvature Flow, Image Enhancement, and Shape Recovery in Medical Images," in *Visualization and Mathematics*, H. Hege and K. Poltheir, Eds. New York: Springer, 1997, pp. 329-345.

[70] C. Corsi, G. Saracino, A. Sarti, and C. Lamberti, "Left ventricular volume estimation for real-time three- dimensional echocardiography," *IEEE Transactions on Medical Imaging*, vol. 21, pp. 1202-1208, 2002.

[71] A. Yezzi, S. Kichenassamy, A. Kumar, P. Olver, and A. Tannenbaum, "A geometric snake model for segmentation of medical imagery," *IEEE Transactions on Medical Imaging*, vol. 16, pp. 199-209, 1997.

[72] J. Y. Park, T. McInerney, D. Terzopoulos, and M. H. Kim, "A non-self-intersecting adaptive deformable surface for complex boundary extraction from volumetric images," *Computers & Graphics-Uk*, vol. 25, pp. 421-440, 2001.

[73] J. Ivins and J. Porrill, "Active region models for segmenting medical images," presented at IEEE International Conference on Image Processing, Austin, TX, 1994.

[74] R. Ronfard, "Region-Based Strategies for Active Contour Models," *International Journal of Computer Vision*, vol. 13, pp. 229-251, 1994.

[75] R. G. Holt and R. A. Roy, "Measurements of bubble-enhanced heating from focused, MHz-frequency ultrasound in a tissue-mimicking material," *Ultrasound in Medicine and Biology*, vol. 27, pp. 1399-1412, 2001.

[76] A. F. Frangi, W. J. Niessen, and M. A. Viergever, "Three-dimensional modeling for functional analysis of cardiac images: A review," *IEEE Transactions on Medical Imaging*, vol. 20, pp. 2-25, 2001.

[77] L. Rosenberg, "Virtual fixtures: perceptual tools for telerobotic manipulation," presented at IEEE Virtual Reality Annual International Symposium, 1993.

[78] S. Ho, R. Hibberd, and B. Davies, "Robot assisted knee surgery," *IEEE Eng Med Biol*, vol. 14, pp. 292-300, 1995.

[79] S. Park, R. Howe, and D. Torchiana, "Virtual fixtures for robot-assisted minimally-invasive cardiac surgery," in *MICCAI 2001*, vol. 2208, *LNCS*, W. Niessen and M. Viergever, Eds. Berlin: Springer-Verlag, 2001, pp. 1419-20.

[80] P. L. Gleason, R. Kikinis, D. Altobelli, W. Wells, E. Alexander, 3rd, P. M. Black, and F. Jolesz, "Video registration virtual reality for nonlinkage stereotactic surgery," *Stereotact Funct Neurosurg*, vol. 63, pp. 139-43, 1994.

[81] Y. Sato, M. Nakamoto, Y. Tamaki, T. Sasama, I. Sakita, Y. Nakajima, M. Monden, and S. Tamura, "Image guidance of breast cancer surgery using 3-D ultrasound images and augmented reality visualization," *IEEE Trans Med Imaging*, vol. 17, pp. 681-93, 1998.

[82] A. Gronningsaeter, A. Kleven, S. Ommedal, T. E. Aarseth, T. Lie, F. Lindseth, T. Lango, and G. Unsgard, "SonoWand, an ultrasound-based neuronavigation system," *Neurosurgery*, vol. 47, pp. 1373-9; discussion 1379-80, 2000.

[83] J. Ellsmere, J. Stoll, D. Rattner, D. Brooks, R. Kane, W. I. Wells, R. Kikinis, and K. Vosburgh, "Visualizing laparoscopic ultrasound images in the context of preoperative CT can facilitate interpretation," presented at Society of American Gastrointestinal Endoscopic Surgeons, Los Angeles, CA, 2003.

[84] D. Aiger and D. Cohen-Or, "Mosaicing ultrasonic volumes for visual simulation," *IEEE Computer Graphics and Applications*, vol. 20, pp. 53-61, 2000.

[85] A. Moskalik, P. L. Carson, C. R. Meyer, J. B. Fowlkes, J. M. Rubin, and M. A. Roubidoux, "Registration of three-dimensional compound ultrasound scans of the breast for refraction and motion correction," *Ultrasound Med Biol*, vol. 21, pp. 769-78, 1995.

[86] R. N. Rohling, A. H. Gee, and L. Berman, "Three-dimensional spatial compounding of ultrasound images," *Med Image Anal*, vol. 1, pp. 177-193, 1996/7.

[87] J. F. Krucker, C. R. Meyer, G. L. LeCarpentier, J. B. Fowlkes, and P. L. Carson, "3D spatial compounding of ultrasound images using image-based nonrigid registration," *Ultrasound Med Biol*, vol. 26, pp. 1475-88, 2000.

[88] P. Zerfass, C. D. Werner, F. B. Sachse, and O. Dössel, "Deformation of surface nets for interactive segmentation of tomographic data," presented at Biomedical Technology Conference 2000, Luebeck, Germany, 2000.

[89] http://www-ibt.etec.uni-karlsruhe.de/research/activecontours/.

[90] L. N. Trefethen and D. I. Bau, *Numerical Linear Algebra*. Philadelphia: SIAM, 1997.

[91] M. H. Syn, "Model-based three-dimensional freehand ultrasound imaging," in *Engineering*. Cambridge, UK: Cambridge University, 1996.

[92] S. Pieper, M. Weidenbach, and T. Berlage, "Registration of 3D ultrasound images to surface models of the heart," presented at Interface to real & virtual worlds, Montpellier, France, 1997.

[93] T. Makela, P. Clarysse, O. Sipila, N. Pauna, Q. C. Pham, T. Katila, and I. E. Magnin, "A review of cardiac image registration methods," *IEEE Trans Med Imaging*, vol. 21, pp. 1011-21, 2002.

[94] M. H. Syn, R. W. Prager, and L. H. Berman, "Bayesian registration of models using finite element eigenmodes," *Int J Med Inf*, vol. 45, pp. 145-62, 1997.

[95] A. S. Gopal, Z. Q. Shen, P. M. Sapin, A. M. Keller, M. J. Schnellbaecher, D. W. Leibowitz, O. O. Akinboboye, R. A. Rodney, D. K. Blood, and D. L. King, "Assessment of Cardiac-Function by 3-Dimensional Echocardiography Compared with Conventional Noninvasive Methods," *Circulation*, vol. 92, pp. 842-853, 1995.

[96] G. Armstrong, L. Cardon, D. Vilkomerson, D. Lipson, J. Wong, L. L. Rodriguez, J. D. Thomas, and B. P. Griffin, "Localization of needle tip with color doppler during pericardiocentesis: In vitro validation and initial clinical application," *J Am Soc Echocardiogr*, vol. 14, pp. 29-37, 2001.

[97] R. Howe and Y. Matsuoka, "Robotics for Surgery," *Annu Rev Biomed Eng*, vol. 1, pp. 211-40, 1999.

[98] P. Abolmaesumi, S. E. Salcudean, W. H. Zhu, M. R. Sirouspour, and S. P. DiMaio, "Image-guided control of a robot for medical ultrasound," *IEEE Transactions on Robotics and Automation*, vol. 18, pp. 11-23, 2002.

[99] M. Song, R. M. Haralick, F. H. Sheehan, and R. K. Johnson, "Integrated surface model optimization for freehand three-dimensional echocardiography," *IEEE Trans Med Imaging*, vol. 21, pp. 1077-90, 2002.

[100] W. M. Wells, 3rd, P. Viola, H. Atsumi, S. Nakajima, and R. Kikinis, "Multi-modal volume registration by maximization of mutual information," *Med Image Anal*, vol. 1, pp. 35-51, 1996.

[101] A. C. S. Chung, W. M. Wells, A. Norbash, and W. E. L. Grimson, "Multi-modal image registration by minimising Kullbach-Leibler distance," in *MICCAI 2002*, vol. LNCS 2489, T. Dohi and R. Kikinis, Eds. Tokyo, Japan: Springer, Berlin, 2002, pp. 525-532.